Eur. J. Mineral.
2016, **28**, 105–123
Published online 23 September 2015

Special issue dedicated to Thomas Armbruster

Silicocarnotite, $Ca_5[(SiO_4)(PO_4)](PO_4)$, a new „old" mineral from the Negev Desert, Israel, and the ternesite–silicocarnotite solid solution: indicators of high-temperature alteration of pyrometamorphic rocks of the Hatrurim Complex, Southern Levant

EVGENY V. GALUSKIN[1,*], IRINA O. GALUSKINA[1], FRANK GFELLER[2], BILJANA KRÜGER[3], JOACHIM KUSZ[4], YEVGENY VAPNIK[5], MATEUSZ DULSKI[6] and PIOTR DZIERŻANOWSKI[7]

[1] Department of Geochemistry, Mineralogy and Petrography, Faculty of Earth Sciences, University of Silesia, Będzińska 60, 41–200 Sosnowiec, Poland
*Corresponding author, e-mail: evgeny.galuskin@us.edu.pl
[2] Mineralogical Crystallography, Institute of Geological Sciences, University of Bern, Freiestrasse 3, 3012 Bern, Switzerland
[3] Institute of Mineralogy and Petrography University of Innsbruck, Innrain 52, 6020 Innsbruck, Austria
[4] Institute of Physics, University of Silesia, Uniwersytecka 4, 40–007 Katowice, Poland
[5] Department of Geological and Environmental Sciences, Ben-Gurion University of the Negev, POB 653, Beer-Sheva 84105, Israel
[6] Silesian Center for Education and Interdisciplinary Research, Institute of Material Science, 75 Pułku Piechoty 1a, 41–500 Chorzow, Poland
[7] Institute of Geochemistry, Mineralogy and Petrology, Warsaw University, al. Żwirki i Wigury 93, 02–089 Warszawa, Poland

Abstract: The new mineral silicocarnotite, $Ca_5[(SiO_4)(PO_4)](PO)_4$ (*Pnma*; $a = 6.72230(1)$, $b = 15.4481(2)$, $c = 10.0847(2)$ Å; $V = 1047.37(2)$ Å^3, $Z = 4$), has been discovered in pyrometamorphic gehlenite-bearing rocks of the Hatrurim Complex, Negev Desert, Israel. The name "silicocarnotite" has been used for the synthetic phase $Ca_5[(SiO_4)(PO_4)](PO)_4$ for more than 100 years. The holotype specimen is a gehlenite–fluorapatite rock with minor andradite and pseudowollastonite. Silicocarnotite is colourless with a white streak and a vitreous lustre. The microhardness is $VHN_{50} = 523$–552 kg m^{-2}, mean = 537 kg m^{-2}. Mohs hardness is about 5. Cleavage and parting are not observed. The calculated density is 3.06 g cm^{-3}. Silicocarnotite is biaxial (+), with $\alpha = 1.618(2)$, $\beta = 1.621(2)$, $\gamma = 1.628(2)$ (589 nm), 2V (meas.) = 75(5)°, $2V_Z$ (calc.) = 67°; dispersion is medium, $r >$ v; the orientation is $X \parallel \mathbf{b}$, $Y \parallel \mathbf{a}$, $Z \parallel \mathbf{c}$; the mineral is nonpleochroic. The empirical formula of holotype silicocarnotite is $Ca_{5.011}Sr_{0.006}P_{1.774}Si_{1.106}S^{6+}_{0.113}O_{12}$. The strongest diffraction lines are [d_{hkl}, (I)]: 2.815 (100), 2.596 (62), 2.575 (50), 3.285 (48), 3.903 (40), 3.007 (39), 3.176 (36), 1.746 (29), 3.082 (29).

Minerals of the silicocarnotite–ternesite solid solution, $Ca_5[(SiO)_4(PO_4)](PO)_4$–$Ca_5(SiO_4)_2SO_4$, occur in larnite- and gehlenite-bearing pyrometamorphic rocks of the Hatrurim Complex, distributed in the Dead Sea rift area on the territories of Israel, Palestine and Jordan. New data on morphology, composition, structure, mineral associations, mechanisms and conditions of growth of the ternesite–silicocarnotite solid-solution series are presented. Large ternesite porphyroblasts (metacrysts) in fine-grained larnite–ye'elimite matrix are the most striking evidence for high-temperature alterations of early "clinker minerals". Silicocarnotite–ternesite grains grew as a result of reactions between primary pyrometamorphic minerals (larnite, flamite, fluorellestadite–fluorapatite) with sulphate-bearing melts, which are side-products of the combustion processes during the pyrometamorphism.

Key-words: Silicocarnotite; new mineral; P-bearing ternesite; solid solution; crystal structure; Raman; metacrysts; calcium silicophosphate; pyrometamorphism; combustion processes; Hatrurim Complex.

Introduction

Silicocarnotite, $Ca_5[(SiO_4)(PO_4)](PO)_4$ (*Pnma*; $a = 6.72230(1)$, $b = 15.4481(2)$, $c = 10.0847(2)$ Å; $V = 1047.37(2)$ Å^3, $Z = 4$), was detected in samples of pyrometamorphic gehlenite-bearing rocks of the Hatrurim Complex. The studied samples are represented by semi-manufactured stone artefacts found at Palaeolithic stone-

DOI: 10.1127/ejm/2015/0027-2494

0935-1221/15/0027-2494 $ 8.55

tool workshops on the eastern slope of the Har Parsa (31°12′31″N 35°17′09″E) and near Tsomet Hatrurim (31°12′58″N 35°15′48″E). The two localities are situated between Arad and the Dead Sea, Negev Desert, Israel (Vapnik & Vardi, 2013; Vapnik *et al*., 2015).

Silicocarnotite (silico-carnotite) is a historical name used for more than 100 years for the orthorhombic artificial phase $Ca_5(PO_4)_2(SiO)_4$ or $Ca_5[(SiO)_4(PO_4)](PO)_4$. This phase was first described from basic slags by Carnot & Richard (1883). The name silicocarnotite goes back to Kroll (1911) and was subsequently used by several authors (Riley & Segnit, 1949; Trömmel & Zaminer, 1959; Keppler, 1968, *etc*.). Nowadays the name is well established and used for synthetic $Ca_5(PO_4)_2(SiO)_4$ (Gualtieri *et al*., 2008; Radev *et al*., 2009; Gomes *et al*., 2011; Martínez *et al*., 2012; Roh *et al*., 2012; Yu *et al*., 2013), even if the name is unfortunate, because the mineral carnotite, $K_2(UO_2)_2(VO_4)_2 \cdot 3H_2O$ (Friedel & Cumenge, 1899; Sundberg & Sillén, 1949) bears no relation to silicocarnotite. The crystal structure of silicocarnotite was first solved by Dickens & Brown (1971). Silicocarnotite is a structural analogue of ternesite, $Ca_5(SiO_4)_2SO_4$ (*Pnma*; $a = 6.863(1)$, $b = 15.387(1)$, $c = 10.181(1)$ Å; $V = 1075.1(1)$, $Z = 4$), which was found in altered xenoliths in volcanic rocks of the Bellerberg, Eifel, Germany (Irran *et al*., 1997). The artificial analogue of ternesite was described from oil-shale slags at Lapanouse-de-Sévérac, Aveyron, Midi-Pyrénées, France (Eytier *et al*., 2004; Gatel *et al*., 2015).

Minerals of the silicocarnotite-ternesite solid solution commonly occur in larnite- and occasionally in gehlenite-bearing pyrometamorphic rocks of the Hatrurim Complex, distributed in the Dead Sea rift area of Southern Levant in the territories of Israel, Palestine and Jordan. The pyrometamorphic rocks of the Hatrurim-Complex are spread over many square kilometres. Their formation is driven by combustion processes of a sedimentary protolith (Bentor, 1960; Gross, 1977; Vapnik *et al*., 2007; Novikov *et al*., 2013) but the genesis of the Hatrurim Complex is still under discussion (Sokol *et al*., 2010; Kolodny *et al*., 2013; Vapnik & Novikov, 2013). The main hypothesis is pyrometamorphic rock-formation due to combustion of organic matter (bitumen) contained in primary sedimentary rocks (Kolodny & Gross, 1974; Matthews & Gross, 1980; Geller *et al*., 2012). Recently a ''mud-volcanic'' hypothesis has been proposed, suggesting high-temperature pyrometamorphic alteration of primary rocks driven by methane fire exhaling from tectonic active zones of the Dead Sea rift (Sokol *et al*., 2010; Novikov *et al*., 2013). All hitherto suggested models comprise two main stages of rock alteration: (1) a high-temperature pyrometamorphic stage, forming H_2O-free mineral associations analogue to Portland-cement clinker production; this first stage is described as a dry, isochemical process; (2) a low-temperature hydrothermal and weathering stage, which is accompanied by zeolitization, hydration and secondary carbonation of the high-temperature mineral associations (Kolodny & Gross, 1974; Matthews & Gross, 1980; Geller *et al*., 2012; Kolodny *et al*., 2014; Sokol *et al*., 2014).

The genetic hypotheses are mainly based on mineralogical studies of rocks from the Hatrurim Complex carried out in the 1960–1970s (Gross, 1977). Surprisingly, a great number of rock-forming and accessory minerals have not been identified until the past 5 years, during which several new minerals have been described: fluormayenite $Ca_{12}Al_{14}O_{32}F_2$ and fluorkyuygenite $Ca_{12}Al_{14}O_{32}[(H_2O)_4F_2]$ (Galuskin *et al*., 2015a), silicocarnotite $Ca_5[(SiO_4)(PO_4)](PO_4)$ (this paper), nabimusaite $KCa_{12}(SiO_4)_4(SO_4)O_2F$ (Galuskin *et al*., 2015b), barioferrite (Murashko *et al*., 2011), shulamitite $Ca_3TiFeAlO_8$ (Sharygin *et al*., 2013), zadovite $BaCa_6[(SiO_4)(PO_4)](PO_4)_2F$ and aradite $BaCa_6[(SiO_4)(VO_4)](VO_4)_2F$ (Galuskin *et al*.. 2015c), gurimite (Galuskina *et al*., 2013), vapnikite Ca_3UO_6 (Galuskin *et al*., 2014), harmunite $CaFe_2O_4$ (Galuskina *et al*., 2014a), khesinite $Ca_4(Mg_3Fe^{3+}{}_9)O_4(Si_3Fe^{3+}{}_9)O_{36}$ (Galuskina *et al*., 2014b), murashkoite FeP, halamishite Ni_5P_4, zuktamrurite FeP_2, negevite NiP_2, transjordanite Ni_2P (Britvin *et al*., 2015). In addition, many minerals from Hatrurim Complex rocks were reported as second world occurrence: chlormayenite $Ca_{12}Al_{14}O_{32}Cl_2$, chlorkyuygenite $Ca_{12}Al_{14}O_{32}[(H_2O)_4Cl_2]$ (Galuskin *et al*., 2015d), vorlanite (Galuskin *et al*., 2013a), jusmundite $Ca_{11}(SiO_4)_4O_2S$ (Galuskin *et al*., 2015b) and ternesite $Ca_5(SiO_4)_2SO_4$ (Galuskin *et al*., 2013b).

In this article, we give a detailed description of silicocarnotite (IMA2013-139), which comprises new data on morphology, composition, structure, mineral associations, mechanisms and conditions of growth of the ternesite–silicocarnotite solid-solution series from different occurrences in the Negev Desert and Judean Mountains. Moreover, we present data indicating that the pyrometamorphic process is not a single event. A considerable part of the minerals from the early ''clinker association'' of larnite- and gehlenite-bearing rocks of the Hatrurim Complex were subjected in a later stage to alterations at high temperatures.

The type material of silicocarnotite is deposited in the mineralogical collections of the Museum of Natural History in Bern with catalogue number NMBE-42716.

Experimental details

The crystal morphology and chemical composition of the ternesite–silicocarnotite series and associated minerals were examined using optical microscopes, analytical electron scanning microscope Philips XL30 ESEM/EDS/CL (Faculty of Earth Sciences, University of Silesia, Poland), and electron microprobe CAMECA SX100 and CAMECA SXfiveFE (Institute of Geochemistry, Mineralogy and Petrology, University of Warsaw, Poland). Electron probe microanalyses of ternesite–silicocarnotite and associated minerals were performed at 15 kV and 10 nA using the following lines and standards: K$K\alpha$, Al$K\alpha$ - orthoclase; Ba$L\alpha$, S$L\alpha$ - barite, Sr$L\alpha$ - celestine, Cl$K\alpha$ - tugtupite; P$K\alpha$, F$K\alpha$ - apatite; Cr$K\alpha$ - Cr_2O_3; Fe$K\alpha$ - hematite; Mn$K\alpha$ -

rhodonite; Ti$K\alpha$ - rutile; Mg$K\alpha$, Ca$K\alpha$, Si$K\alpha$ - diopside; Na$K\alpha$ - albite.

Single-crystal X-ray studies of silicocarnotite and P-bearing ternesite were carried out using a Bruker APEX II SMART (Mo$K\alpha$, $\lambda = 0.71073$ Å) and SuperNova Dual diffractometer with a mirror monochromator (Mo$K\alpha$, $\lambda = 0.71073$ Å) and Atlas CCD detector (Agilent Technologies) diffractometers (University of Bern, Switzerland and Institute of Physics, University of Silesia, Poland). The structures were solved by direct methods, with subsequent analyses of difference-Fourier maps, and refined with neutral-atom scattering factors using SHELX97 (Sheldrick, 2008).

The powder X-ray pattern of silicocarnotite was measured using a SuperNova Dual diffractometer (Mo$K\alpha$, $\lambda = 0.71073$ Å) (Institute of Physics, University of Silesia, Poland). We obtained powder diffraction data (pseudo-Gandolfi) on the single-crystal grain of silicocarnotite (YV-415) using modern software (Table S1, freely available online as Supplementary Material linked to this article on the GSW website of the journal: http://eurjmin.geoscienceworld.org/); the calculated unit-cell parameters are: $a = 6.73(1)$, $b = 15.44(1)$, $c = 10.09(1)$ Å; $V = 1048.5(2)$ Å^3. Nevertheless, it must be stated that this procedure corresponds to the calculation of a powder diffraction pattern from refined atomic coordinates. Furthermore, the measured pattern was recorded with Mo$K\alpha$ radiation, which leads to substantial reflection overlap; thus individual intensities cannot be assigned. For this reason calculated powder diffraction data for silicocarnotite (in Å for Cu$K\alpha$) are given in Table S2 (POWDER CELL program, Kraus & Nolze, 1996).

Raman spectra of silicocarnotite and ternesite were recorded on a WITec confocal Raman microscope (Institute of Physics, University of Silesia, Poland). The excitation laser radiation was coupled into a microscope through a single-mode optical fibre with a diameter of 50 μm. An air Olympus MPLAN (100×/0.90NA) objective was used. Raman scattered light was focussed onto a multimode fibre (50 μm diameter) and monochromator with a 600 mm^{-1} grating. The power of the laser at the sample position was 44 mW. Some 15–20 scans with integration time of 10–15 s and a resolution of 3 cm^{-1} were collected and averaged. The spectrometer monochromator was calibrated using the Raman scattering line of a silicon plate (520.7 cm^{-1}).

Silicocarnotite, a new mineral from gehlenite rocks of the Hatrurim Complex

Silicocarnotite with chemical composition close to the ideal crystal chemical formula $Ca_5[(SiO)_4(PO_4)](PO)_4$ occurs in gehlenite rocks of the Hatrurim Complex. Outcrops of this rock type have been described from the Judean Mts. and the Negev Desert (Bentor, 1960; Gross, 1977; Vapnik *et al*., 2007; Novikov *et al*., 2013). Silicocarnotite commonly forms symplectites with rankinite, $Ca_3Si_2O_7$, and occasionally with pseudowollastonite. These intimate intergrowths with other minerals caused difficulties for a complete new mineral description (Vapnik *et al*., 2015). The first occurrence of silicocarnotite as a symplectite with pseudowollastonite was detected from gehlenite rocks of Jabel Harmun, Judean Mts., Palestinian Autonomy (Table 1, specimen number IS105).

Grains of silicocarnotite 0.05–0.15 mm in size were found at two localities of the Hatrurim Basin, Negev Desert, which is known as the largest area of Hatrurim Complex outcrops in Israel (Figs 1 and 2). Both silicocarnotite-bearing gehlenite rock specimens are stone artefacts found at Palaeolithic stone-tool workshops

Table 1. Chemical composition of silicocarnotite.

locality	Jabel Harmun			Har Parsa			Tsomet Hatrurim		
sample	IS105			YV-415			YV-567		
wt.%	mean 7	s.d.	range	mean 6	s.d.	range	mean 18	s.d.	range
SO_3	0.93	0.75	0.23–2.22	1.85	0.15	1.62–2.05	0.33	0.16	0.13–0.74
V_2O_5	<0.08			<0.08			0.50	0.10	0.38–0.76
P_2O_5	27.55	1.23	25.50–29.38	25.81	0.36	25.45–26.53	27.82	0.52	26.47–28.56
SiO_2	12.97	0.69	11.96–13.96	13.62	0.10	13.47–13.75	12.74	0.23	12.47–13.13
SrO	0.15			0.13	0.01	0.12–0.15	0.17	0.02	0.13–0.20
CaO	56.84	0.32	56.43–57.22	57.61	0.31	57.16–58.06	57.21	0.27	56.66–57.59
Na_2O	0.05	0.04	0–0.14	<0.02			<0.02		
Total	98.49			99.02			98.77		
Calculated on 12 O									
Ca	4.959			5.011			4.993		
Sr	0.007			0.006			0.008		
Na	0.008								
P	1.899			1.774			1.918		
Si	1.056			1.106			1.038		
S^{6+}	0.057			0.113			0.020		
V^{5+}							0.027		

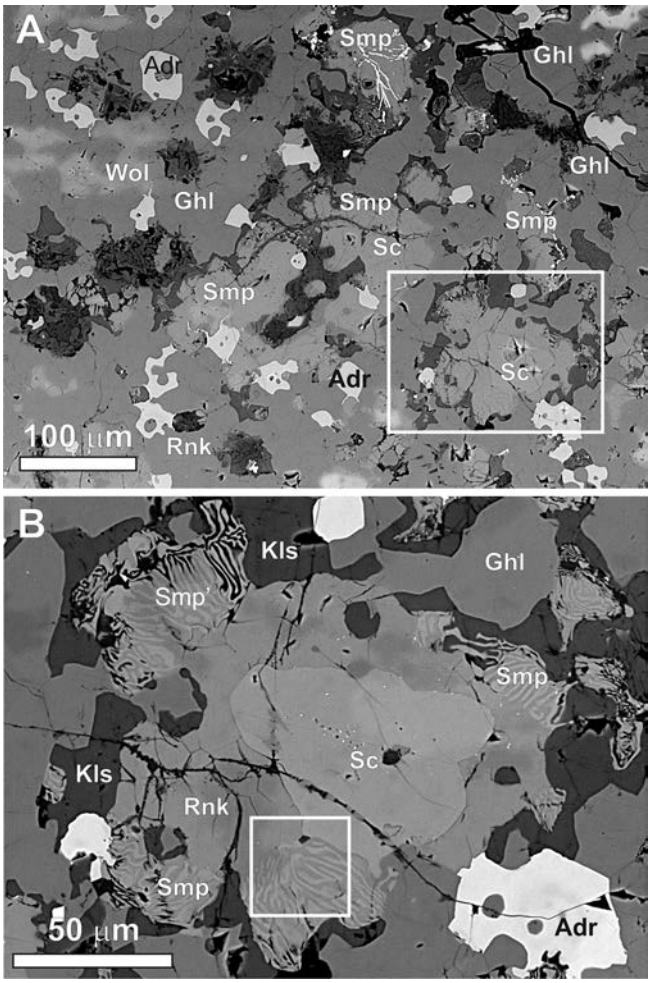

Fig. 1. **A** Gehlenite rock containing silicocarnotite (specimen YV567), a fragment magnified in Fig. 1B is shown by the frame; **B** silicocarnotite grain with rim composed of rankinite and silicocarnotite–rankinite microsymplectite. The fragment, on which Raman mapping (Fig. 10) was performed, is shown by the frame. Adr – andradite, Ghl – gehlenite, Smp – rankinite–silicocarnotite microsymplectite (symplectite sub-individuals up to 1–3 μm in width), Smp' – rankinite–silicocarnotite nanosymplectite (symplectite sub-individuals up to 400–800 nm in width), Rnk – rankinite, Kls – kalsilite, Sc – silicocarnotite, Wol – pseudowollastonite.

located on the eastern slope of the Har Parsa (specimen number YV-415) and near Tsomet Hatrurim (specimen number YV-567). In specimen YV-567, silicocarnotite is a rock-forming mineral together with gehlenite, andradite and rankinite (Fig. 1A). Minor and accessory minerals are represented by pseudowollastonite, fluorapatite, kalsilite, magnesioferrite–jacobsite, and also lamellar intergrowths of larnite and flamite. In this specimen, silicocarnotite forms heterogeneous and porous grains about 0.05 mm in size. The latter are overgrown by a rim of rankinite–silicocarnotite microsymplectites (Fig. 1B). The holotype specimen YV-415 is a gehlenite–fluorapatite rock with minor andradite and pseudowollastonite. In this rock silicocarnotite is a rare mineral, forming spherulitic aggregates on the walls of

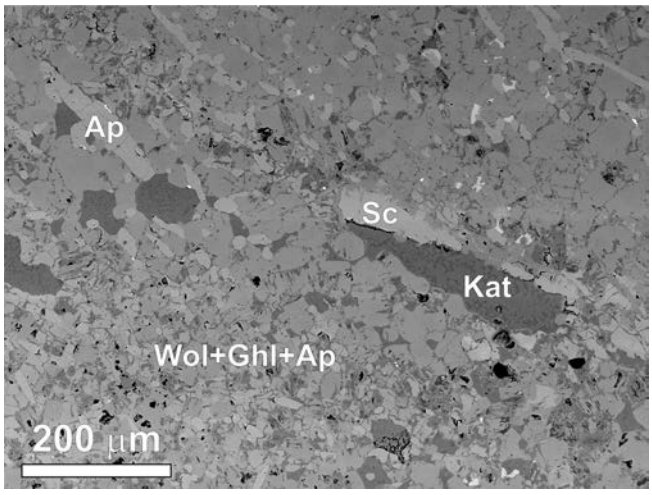

Fig. 2. Rare silicocarnotite grains incrusting walls of small cavities filled with katoite and Ca-hydrosilicates. Ap – fluorapatite, Wol – pseudowollastonite, Sc – silicocarnotite, Ghl – gehlenite, Kat – katoite.

small cavities filled with katoite and Ca-hydrosilicates (Fig. 2). A homogeneous grain of silicocarnotite was extracted from this specimen and used for chemical, structural and optical studies. Chemical composition and microhardness were also measured on specimen YV-567, which is a co-type for silicocarnotite. Moreover, a Raman mapping of the symplectites was performed on this sample.

Silicocarnotite is a colourless, transparent mineral with white streak and vitreous lustre. The mineral does not fluoresce under ultraviolet rays or the electron beam. The microhardness, VHN load 50 g, ranges from 523 to 552 kg m^{-2}, with a mean ($n = 14$) of 537 kg m^{-2}, corresponding to a Mohs hardness of about 5. No cleavage or parting is observed. Silicocarnotite shows an uneven fracture and is brittle. The density was not measured due to the small grain-size and high porosity of silicocarnotite. The calculated densities based on microprobe analyses and relevant structural data are in good agreement: 3.064 g cm^{-3} (specimen YV-567); 3.062 g cm^{-3} (specimen YV-415). Silicocarnotite is biaxial (+), with $\alpha = 1.618(2)$, $\beta = 1.621(2)$, $\gamma = 1.628(2)$ (589 nm), 2V (meas.) = 75(5)°, $2V_Z$ (calc.) = 67°, dispersion $r >$ v is medium, the orientation is $X \parallel \mathbf{b}$, $Y \parallel \mathbf{a}$, $Z \parallel \mathbf{c}$. The mineral is colourless in thin-section and nonpleochroic.

The following empirical formulae were obtained for silicocarnotite on the basis of 12 O atoms per formula unit (*apfu*): Jabel Harmun (IS105) - $Ca_{4.959}Na_{0.008}Sr_{0.007}P_{1.899}Si_{1.056}S^{6+}_{0.057}O_{12}$; Har Parsa (YV-415, holotype) - $Ca_{5.011}Sr_{0.006}P_{1.774}Si_{1.106}S^{6+}_{0.113}O_{12}$; Tsomet Hatrurim (YV-567, co-type) - $Ca_{4.988}Sr_{0.008}P_{1.924}Si_{1.033}V^{5+}_{0.027}S^{6+}_{0.020}O_{12}$ (Table 1). The simplified formula of natural silicocarnotite can be written as $Ca_5(P_{1.8\text{-}2.0}Si_{1\text{-}1.1}S_{0\text{-}0.1})_{\Sigma 3}O_{12}$. Taking into account the sites in the crystal structure (see structural data below), the end-member crystal chemical formula may be written as $Ca_5[(PO_4)(SiO_4)](PO_4)$.

Minerals of the ternesite–silicocarnotite series from larnite rocks of the Hatrurim Complex

In larnite pyrometamorphic rocks of the Hatrurim Complex, minerals of the ternesite $Ca_5(SiO_4)_2(SO_4)$ (*Trn*) – silicocarnotite $Ca_5[(SiO_4)(PO_4)](PO_4)$ (*Sc*) solid solution occur. Their composition varies in the range $Trn_{0.92}Sc_{0.08}$–$Sc_{0.60}Trn_{0.40}$ (Fig. 3; Tables 2–4). Rocks containing minerals of the ternesite–silicocarnotite series were studied from the following localities: Nahal Darga, Jabel Harmun, Nabi Musa, Ma'ale Adummin (Judean Mts., Palestinian Autonomy) and from Gurim Upland and Har Parsa in the Negev Desert (Israel) (Figs 4, 5A, B; 6A–C). The geological setting of these localities has been described in detail by Novikov *et al*. (2013) and Galuskina *et al*. (2014a). Well-formed crystals of ternesite and their aggregates are widespread and irregularly distributed in fine-grained larnite nodules of pseudoconglomerates. The diameter of these nodules ranges from several up to tens of centimetres. In the following, the term porphyroblast (or metacryst) will refer to such well-formed crystals growing in a fine-grained solid substrate. The name 'pseudoconglomerates' was introduced by Gross (1977; 1984) and refers to strongly altered rocks of the Hatrurim Complex composed of larnite nodules ('pebbles'; Fig. 4A). Peripheral, concentric cracks filled with secondary hydrosilicates, ettringite-group minerals, carbonates and rarely zeolites are characteristic for such larnite nodules (Fig. 4A, inset). The mineral content of ternesite-bearing larnite nodules from different localities stays similar. The main minerals are larnite and ye'elimite, minerals of the fluorellestadite–-fluorapatite series and their hydroxyl analogues, and of the brownmillerite–srebrodolskite and magnesioferrite–spinel (+magnesiochromite) series. Rarely, minerals of the mayenite group, gehlenite, oldhamite, spurrite and shulamitite appear in this association. Barite, vapnikite, vorlanite, Cu-sulphides and rarely Fe-sulphides are typical accessory minerals.

Ternesite porphyroblasts are unevenly distributed in larnite nodules, from a few metacrystals up to rock-forming (Fig. 6A–C). Ternesite differs little from fluorellestadite–fluorapatite and larnite in back-scattered electron (BSE) images (Fig. 5C), but it is easily discernible in optical microscopy (Fig. 5A, B) and cathodoluminescence (Fig. 6A–C). The largest crystals of ternesite, up to 2 cm in length, were found in brown larnite nodules about 10–15 cm in diameter from Jabel Harmun (Figs 5A, B; 6A). Showy ternesite porphyroblasts are conspicuous on the fresh fractures of larnite nodules (Fig. 4B, C). These specimens have been found in a 10–12 m thick lens of larnite pseudoconglomerate on the west slope of Har Parsa Mt. (Fig. 4A). Ternesite porphyroblasts from Har Parsa are characterized by a shiny surface, with knitted microrelief (Fig. 4C). These metacrysts contain inclusions of ye'elimite and spinel (Fig. 5C). In thin-sections, ternesite metacrysts may easily be distinguished by their low porosity compared to the fine-grained larnite aggregates with isometric ye'elimite and elongated fluorellestadite grains (Fig. 5C). It is noteworthy that, although fluorellestadite is abundant in these larnite nodules (Fig. 5C), it does not occur as inclusions in ternesite. Examination of the grain boundaries between larnite and ternesite shows a phase that appears dark grey in BSE images (Fig. 5E, F). Its EDS spectrum is similar to that of calciolangbeinite $Ca_2K_2(SO_4)_3$.

In larnite nodules from Har Parsa, small, linear zones up to 1 cm in thickness bear large ternesite crystals. Within these zones, ternesite occurs as spherulites together with calciolangbeinite and barite (Fig. 7). In the same samples, cavities produced by gaseous bubbles are now encrusted by small larnite, ye'elimite, fluorellestadite and spinel crystals. The cavities are associated with big grains of calciolangbeinite. Aggregates of well-formed ternesite crystals, isometric spinel and ye'elimite (Fig. 7B) occur in cavities with partially dissolved calciolangbeinite. Moreover, aphthitalite $K_3Na(SO_4)_2$, arcantite K_2SO_4 and sylvite KCl occur together with calciolangbeinite.

In general ternesite porphyroblasts and their aggregates, together with larnite, are the dominating phase in nodules, which usually give the characteristic green colour to the rock. These green ternesite nodules, up to 1–5 cm in size, are found at Jabel Harmun, where they are concentrated in a fragmented horizon (Figs 4D, 6C). Granular aggregates of ternesite from Jabel Harmun, Nahal Darga and East Gurim are commonly associated with nabimusaite $KCa_{12}(SiO_4)_4(SO_4)_2O_2F$ and the potentially new mineral $BaCa_6(SiO_4)_2(SO_4)_2O$, isostructural with zadovite $BaCa_6[(SiO_4)(PO_4)]_2(PO_4)_2F$ (Galuskin *et al*., 2015c).

The porphyroblasts of ternesite from the pyrometamorphic rocks of the Hatrurim Complex contain phosphorus, in contrast to the holotype ternesite from Germany (Irran *et al*., 1997), implying solid solution toward silicocarnotite. The P_2O_5 contents range from 2.5 to 9 wt.%, which corresponds to $Trn_{0.92}Sc_{0.08}$–$Trn_{0.70}Sc_{0.30}$ (Table 1). Ternesite porphyroblasts exhibit a weak chemical zonation with a P-rich central zone, which correlates with a weakening of the cathodoluminescence intensity (Fig. 6A, B). The ternesite crystals are commonly surrounded by P-poor (~ 3 % P_2O_5) rims approximately 1 μm in size (Fig. 6B, C). The correlation between P-content

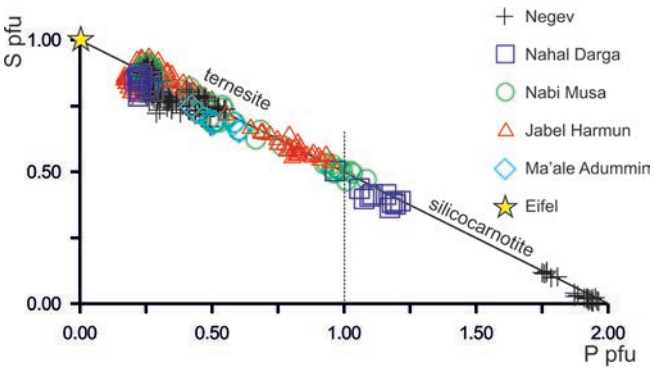

Fig. 3. The ternesite–silicocarnotite solid solution: EMP point analyses projected on the P *vs*. S *apfu* diagram.

Table 2. Chemical composition of ternesite porphyroblast from larnite pyrometamorphic rock, Hatrurim Complex.

locality	Jabel Harmun			Gurim			Har Parsa			Har Parsa			Jabel Harmun			Ma'ale Adummin		
sample	YV654			IS60			ZP-4A			ZP-10A			IS99			MA-6A		
wt.%	mean 20	s.d.	range	34	s.d.	range	10	s.d.	range	44	s.d.	range	27	s.d.	range	8	s.d.	range
CrO_3	0.19	0.06	0.12–0.32	<0.05			0.24	0.04	0.17–0.30	0.22	0.06	0.09–0.33	<0.05			0.35	0.05	0.28–0.43
SO_3	13.72	0.41	12.63–14.38	14.61	0.31	14.01–15.36	12.85	0.42	12.21–13.68	12.68	0.59	11.16–13.59	13.78	0.58	12.81–14.84	11.55	0.48	10.93–12.46
V_2O_5	<0.07			<0.07			0.19	0.06	0.06–0.28	<0.07			0.16	0.07	0.05–0.30	0.13	0.04	0.05–0.19
P_2O_5	2.94	0.39	2.45–3.74	3.80	0.29	3.42–4.55	4.79	0.45	3.78–5.39	4.93	1.05	3.40–7.23	5.56	0.99	3.95–7.43	7.66	0.99	6.20–8.96
TiO_2	0.28	0.06	0.16–0.39	0.31	0.10	0.10–0.51	0.15	0.06	0.07–0.27	0.54	0.13	0.33–0.78	0.18	0.04	0.12–0.28	0.30	0.05	0.23–0.40
SiO_2	24.21	0.37	23.52–24.93	22.72	0.20	22.39–23.10	23.55	0.59	22.34–24.48	23.20	0.80	21.69–24.52	22.01	0.52	21.04–22.92	21.91	0.42	21.16–22.49
Fe_2O_3	0.17	0.14	0–0.52	<0.06			0.07	0.02	0.04–0.15	0.12	0.07	0–0.28	<0.07			0.11	0.07	0–0.23
Al_2O_3	<0.02			<0.02			0.02	0.06	0–0.21	0.14	0.03	0.09–0.20	0.03	0.01	0–0.05	0.25	0.06	0.15–0.33
SrO	<0.08			<0.08			<0.06			<0.07			<0.07			<0.07		
CaO	57.45	0.30	56.82–57.96	58.17	0.30	57.50–58.72	57.73	0.29	57.17–58.06	57.68	0.30	57.14–58.70	58.43	0.35	57.25–59.00	57.71	0.23	57.32–58.09
MgO	0.06	0.01	0.04–0.09	0.06	0.02	0.03–0.10	<0.02			<0.02			0.03	0.01	0–0.05	0.02	0.01	0–0.05
Na_2O	0.09	0.02	0.05–0.13	0.07	0.03	0–0.08	0.05	0.02	0.01–0.09	0.13	0.03	0.06–0.19	0.11	0.03	0.06–0.16	0.11	0.02	0.08–0.14
Total	99.10			99.74			99.65			99.64			100.27			100.07		
Calculated on 12 O																		
Ca	4.984			5.009			4.976			4.983			5.004			4.952		
Sr																		
Mg	0.007			0.007									0.003			0.002		
Na	0.014			0.011			0.007			0.020			0.017			0.017		
X	*5.005*			*5.027*			*4.983*			*5.003*			*5.024*			*4.971*		
Si	1.960			1.826			1.895			1.870			1.759			1.754		
S^{6+}	0.833			0.881			0.776			0.767			0.827			0.694		
P	0.201			0.259			0.327			0.336			0.376			0.519		
Al							0.002			0.013			0.002			0.023		
Ti^{4+}	0.017			0.019			0.009			0.033			0.011			0.018		
V^{5+}							0.010						0.008			0.007		
Cr^{6+}	0.009						0.012			0.011						0.017		
Fe^{3+}	0.010						0.004			0.007						0.006		
T	*3.030*			*2.985*			*3.035*			*3.037*			*2.983*			*3.038*		

Table 3. Chemical composition of ternesite grains from pyrometamorphic rocks.

locality	Jabel Harmun			Nahal Darga			Jabel Harmun			Nabi Musa			Nabi Musa			Gurim		
sample	JBB12			DR-2A			IS93			NM5-1			NM5b			EG4		
wt.%	mean 7	s.d.	range	15	s.d.	range	15	s.d.	range	12	s.d.	range	12	s.d.	range	16	s.d.	range
CrO_3	0.17	0.05	0.09–0.24	0.28	0.04	0.21–0.34	0.22	0.05	0.10–0.27	<0.05			<0.05			0.34	0.03	0.29–0.39
SO_3	13.72	0.34	14.22–15.29	13.90	0.39	13.27–14.70	14.83	0.50	13.65–15.61	13.97	0.39	13.27–14.63	12.69	0.57	11.47–13.74	12.70	0.42	12.10–13.40
V_2O_5	<0.07			<0.07			<0.07			<0.07			<0.07			0.18	0.06	0.08–0.37
P_2O_5	3.12	0.21	2.78–3.43	3.49	0.29	3.03–4.13	4.24	0.75	3.19–6.04	5.13	0.62	3.96–6.44	7.09	0.66	6.15–8.10	7.01	0.67	5.88–8.06
TiO_2	0.37	0.12	0.18–0.51	0.45	0.05	0.32–0.56	0.38	0.06	0.30–0.52	0.20	0.07	0.04–0.31	0.24	0.04	0.17–0.31	0.30	0.03	0.22–0.35
SiO_2	23.48	0.46	22.68–23.98	23.76	0.56	22.97–25.24	21.78	0.46	20.66–22.60	22.21	0.43	21.57–22.79	21.72	0.24	21.43–22.13	21.07	0.33	20.65–21.58
Fe_2O_3	0.17	0.12	0–0.39	0.15	0.07	0–0.27	<0.06			0.16	0.04	0.10–0.25	<0.07			<0.07		
Al_2O_3	0.26	0.18	0–0.45	0.39	0.05	0.29–0.46	0.35	0.08	0.17–0.53	0.18	0.15	0–0.37	0.05	0.03	0–0.13	0.02	0.02	0–0.08
SrO	<0.07			<0.08			0.13	0.05	0–0.22	0.24	0.02	0.21–0.29	<0.07			<0.08		
CaO	57.79	0.21	57.51–58.09	57.68	0.22	57.32–58.11	57.98	0.29	57.41–58.40	57.82	0.31	57.46–58.50	57.95	0.29	57.54–58.45	57.03	0.15	56.68–57.28
MgO	0.03	0.02	0–0.06	<0.02			<0.02			<0.02			<0.02			0.06	0.02	0.03–0.09
Na_2O	0.08	0.02	0.06–0.10	0.16	0.03	0.12–0.22	0.10	0.03	0–0.13	0.16	0.02	0.13–0.19	0.14	0.03	0.10–0.18	0.12	0.02	0.09–0.15
Total	99.19			100.25			100.02			100.07			99.89			98.83		
Calculated on 12 O																		
Ca	5.025			4.938			4.976			4.964			4.977			4.946		
Sr							0.006			0.011								
Mg	0.003			0.000												0.007		
Na	0.012			0.024			0.015			0.025			0.021			0.018		
X	*5.040*			*4.962*			*4.997*			*5.000*			*4.998*			*4.971*		
Si	1.906			1.898			1.745			1.779			1.741			1.705		
S^{6+}	0.836			0.833			0.891			0.840			0.763			0.771		
P	0.214			0.236			0.288			0.348			0.481			0.480		
Al	0.025			0.037			0.033			0.017			0.005			0.001		
Ti^{4+}	0.022			0.027			0.023			0.012			0.015			0.019		
V^{5+}																0.010		
Cr^{6+}	0.008			0.013			0.011									0.017		
Fe^{3+}	0.010			0.009						0.010								
T	*3.021*			*3.053*			*2.991*			*3.006*			*3.005*			*3.003*		

Table 4. Chemical composition of ternesite acicular and platy grains.

locality	Nabi Musa (NM)			NM	Nabi Musa			Jabel Harmun			Jabel Harmun			Nabi Musa			Nahal Darga		
sample	NM6			NM5	NM1			JBB10			660			NM5b			DR-2		
wt.%	mean 9	s.d.	range	6	16	s.d.	range	15	s.d.	range	13			12	s.d.	range	10	s.d.	range
CrO_3	0.21	0.08	0.07–0.34	<0.05	0.16	0.04	0.12–0.28	<0.03			<0.06			0.22	0.03	0.17–0.34	0.24	0.05	0.15–0.34
SO_3	10.73	0.46	9.97–11.23	10.67	9.99	0.53	6.71–8.84	9.95	0.52	9.28–10.72	9.32	0.45	8.79–10.39	8.40	0.33	7.70–8.84	6.78	0.63	5.96–8.41
V_2O_5	<0.07			<0.07	0.11	0.05	0.07–0.24	0.27	0.02	0.25–0.30	0.15	0.08	0–0.33	<0.07			0.39	0.06	0.31–0.53
P_2O_5	9.16	0.51	8.08–10.15	10.10	11.23	1.70	9.90–16.15	11.25	0.78	10.01–12.51	12.67	0.78	11.48–13.94	14.54	0.69	13.64–16.15	16.62	0.99	14.30–17.83
TiO_2	0.45	0.08	0.39–0.68	0.32	0.17	0.04	0.05–0.20	0.19	0.01	0.17–0.22	0.19	0.03	0.15–0.26	0.12	0.04	0.06–0.20	0.15	0.05	0.04–0.20
SiO_2	21.54	0.73	20.59–22.59	19.94	20.25	1.61	18.26–23.27	19.46	0.39	18.78–20.17	18.69	0.50	17.90–19.63	18.64	0.20	18.26–18.94	17.91	0.83	16.94–19.16
Fe_2O_3	0.10	0.07	0–0.21	<0.06	<0.07			0.04	0.05	0–0.16	0.04	0.03	0–0.09	<0.06			0.07	0.05	0–0.16
Al_2O_3	0.02	0.02	0–0.05	<0.02	<0.02						0.23	0.06	0.16–0.36	<0.02			<0.02		
BaO	<0.08			<0.08	<0.08			0.04	0.01	0.02–0.06									
SrO	<0.07			0.12	<0.08			0.06	0.02	0.02–0.08	0.12	0.10	0–0.24	<0.07			<0.07		
CaO	57.47	0.23	57.14–57.76	57.55	58.04	0.63	57.18–59.21				57.28	0.62	56.76–58.94	57.99	0.59	57.18–59.60	57.73	0.27	57.38–58.19
MgO	<0.02			<0.02	<0.02			0.03	0.02	0.02–0.08	<0.02			<0.02			0.04	0.02	0.07–0.07
Na_2O	0.13	0.03	0.09–0.18	0.13	0.13	0.07	0.01–0.35	0.05	0.01	0.03–0.08	0.09	0.03	0.03–0.15	0.10	0.04	0.01–0.15	0.07	0.02	0.04–0.12
Total	99.82			98.83	100.07			98.57			98.54			100.01			100.01		
Calculated on 12 O																			
Ca	4.941			5.013	4.987			4.993			4.987			4.979			4.961		
Ba								0.001											
Sr				0.006							0.006								
Mg								0.004									0.004		
Na	0.020			0.020	0.020			0.008			0.014			0.015			0.012		
X	*4.961*			*5.039*	*5.007*			*5.006*			*5.007*			*4.994*			*4.977*		
Si	1.729			1.621	1.624			1.585			1.519			1.494			1.436		
S^{6+}	0.646			0.651	0.601			0.608			0.568			0.505			0.408		
P	0.623			0.695	0.763			0.775			0.871			0.986			1.128		
Al	0.002										0.022								
Ti^{4+}	0.027			0.020	0.010			0.012			0.012			0.007			0.009		
V^{5+}					0.006			0.015			0.008						0.021		
Cr^{6+}	0.010				0.008									0.011			0.012		
Fe^{3+}	0.006							0.002			0.002						0.004		
T	*3.043*			*2.987*	*3.012*			*2.997*			*3.002*			*3.003*			*3.018*		

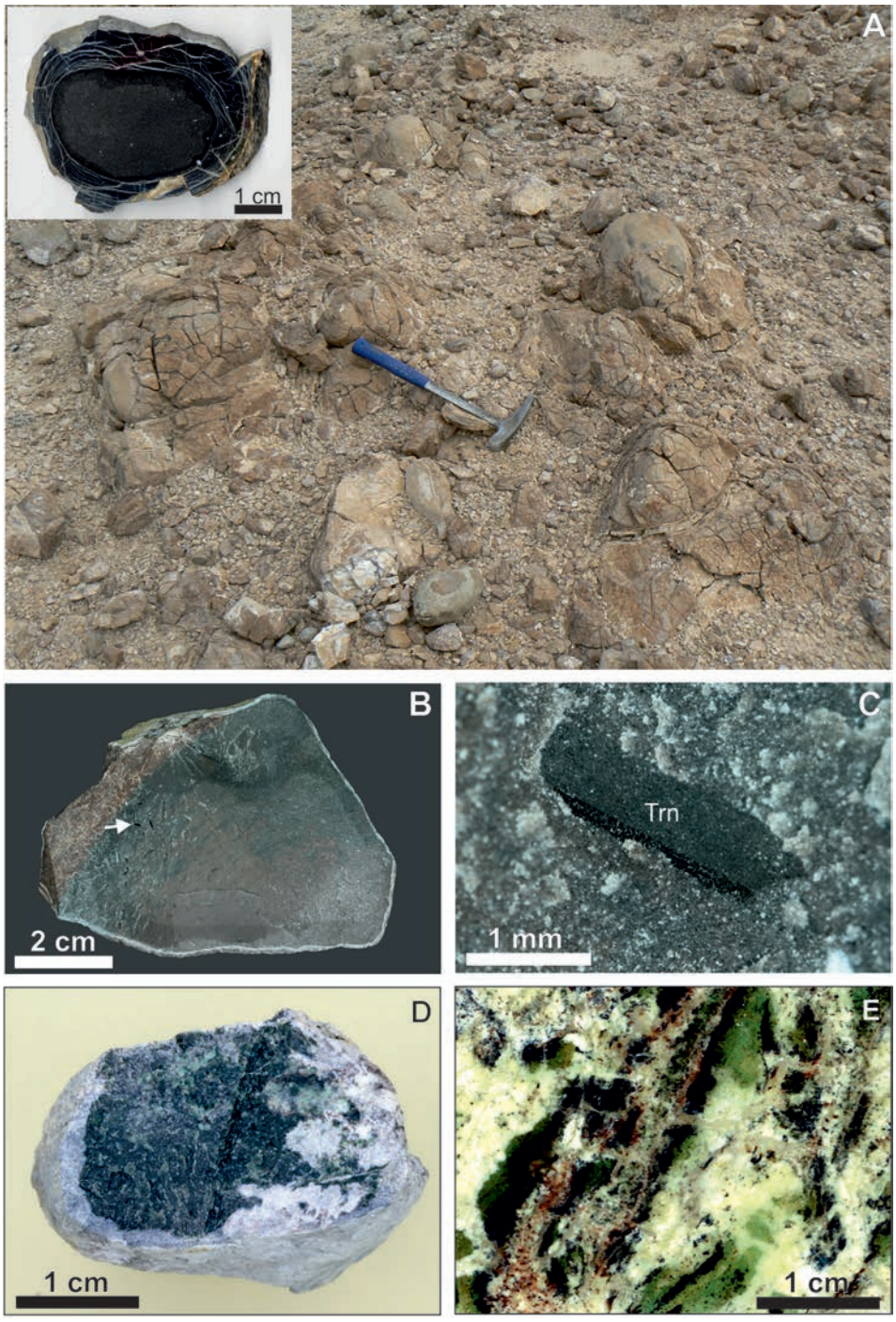

Fig. 4. **A** Outcrop photograph of pseudoconglomerates represented by 'pebbles' of various sizes on the west slope of Har Parsa Mt; the insert shows the typical structure of 'pebble' with characteristic concentric cracks filled with low-temperature minerals; **B** angular 'pebble' from pseudoconglomerate from Har Parsa with visible ternesite porphyroblasts (metacrysts); the crystal magnified in Fig. 4C is shown by arrow; **C** dark-brown ternesite metacrystal with characteristic rough surface; **D** dark-green ternesite 'pebble' from pseudoconglomerate in Jabel Harmun; **E** green fragments of ternesite-rich rock from Nabi Musa.

and luminescence intensity is however questionable and a subject of future research.

Larnite rocks with spherulites of long-prismatic and acicular ternesite–silicocarnotite crystals are restricted to certain areas within the samples (Fig. 6D–F). Ternesite replaces minerals of the fluorellestadite–fluorapatite series (Fig. 6E, F) in inhomogeneous green rocks (Fig. 4E) from the Judean Mts (Nabi Musa, Nahal Darga). The acicular ternesite-silicocarnotite crystals show a wide compositional range (Fig. 3, Table 4): $Trn_{0.70}Sc_{0.30}$ – $Trn_{0.45}Sc_{0.55}$ (Nabi Musa) and $Trn_{0.51}Sc_{0.49}$ – $Trn_{0.40}Sc_{0.60}$ (Nahal Darga). Spherulites of ternesite–silicocarnotite usually

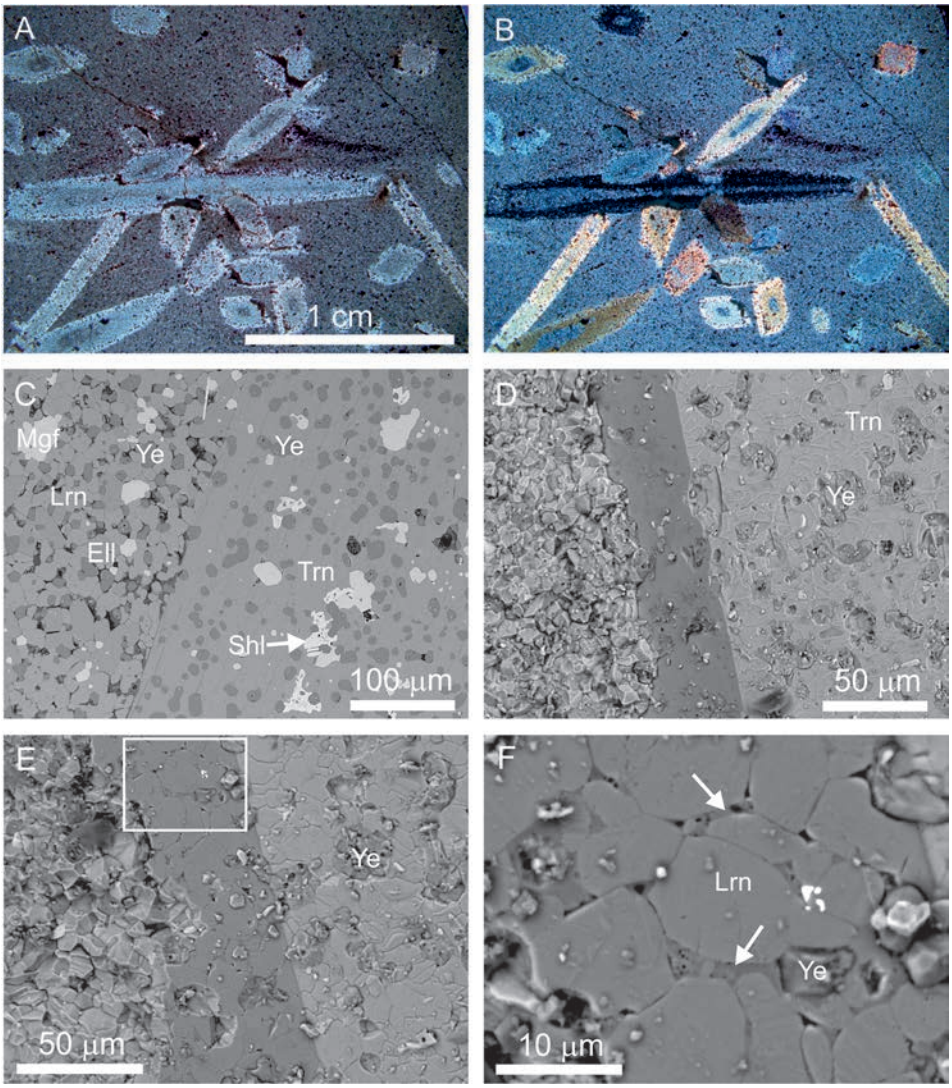

Fig. 5. Ternesite metacrysts from Har Parsa. **A**, **B** Metacrysts in fine-grained larnite–ye'elimite rock, transmitted light, parallel and crossed nicols, respectively; **C** ternesite in fine-grained, porous larnite–fluorellestadite rock, minerals have similar grey colour in BSE image; **D-F** BSE images of fresh fracture: **D** characteristic reticulate microrelief of ternesite metacryst faces with ye'elimite inclusions; **E** imprint of metacryst in rock, fragment magnified in Fig. 5F is shown in frame; **F** grey porous substance between larnite grains, it is easily washed off by water and shows calciolangbeinite composition. Lrn – larnite, Ye – ye'elimite, Shl – shulamitite, Ell- fluorellestadite, Mgf – magnesioferrite, Trn – ternesite.

show weak cathodoluminescence. Similar to the previously discussed metacrysts, the grains within these aggregates show thin zones (~ 1μm) of low-phosphorous ternesite (*ca*. 3–5 wt.% P_2O_5) with a relatively strong luminescence (Fig. 6D).

In some types of larnite and jasmundite (apolarnite) rocks from Jabel Harmun, ternesite replaces flamite exsolution lamellae in larnite (Fig. 8, Table 4). Flamite, $(Ca,Na,K)_2(Si,P)O_4$ (IMA2013-122), is a new mineral (Gfeller *et al*., 2015; Sokol *et al*., 2015) and the natural analogue of the orthorhombic phase $Ca_{15}\square(SiO_4)_6(PO_4)_2$ (a = 21.7310(14), b = 9.3845(6), c = 6.8346(4) Å) (Saalfeld & Klaska, 1981). The structure may be regarded as a P-stabilized high-temperature polymorph of Ca_2SiO_4. While in $Ca_{15}\square(SiO_4)_6(PO_4)_2$ the charge balance is maintained by vacancies on the Ca sites, flamite incorporates monovalent cations according to the scheme: Ca + Si → (Na,K) + P (Gfeller *et al*., 2015). Contents of up to 17 wt.% P_2O_5 have been measured in flamite. The ternesite that replaces flamite is the most P-rich analysed, corresponding to ~$Trn_{0.55\text{-}0.60}Sc_{0.40\text{-}0.45}$ (Table 4).

Raman spectroscopy of silicocarnotite and ternesite

Raman spectra and single-crystal X-ray diffraction data have been collected for silicocarnotite grains of the holotype specimen YV-415 from Har Parsa, Negev (Table 1). The simplified crystal-chemical formula of this crystal is $Ca_5[(P_{0.45}Si_{0.55})O_4]_2[(P_{0.9}S_{0.1})O_4]$. For comparison,

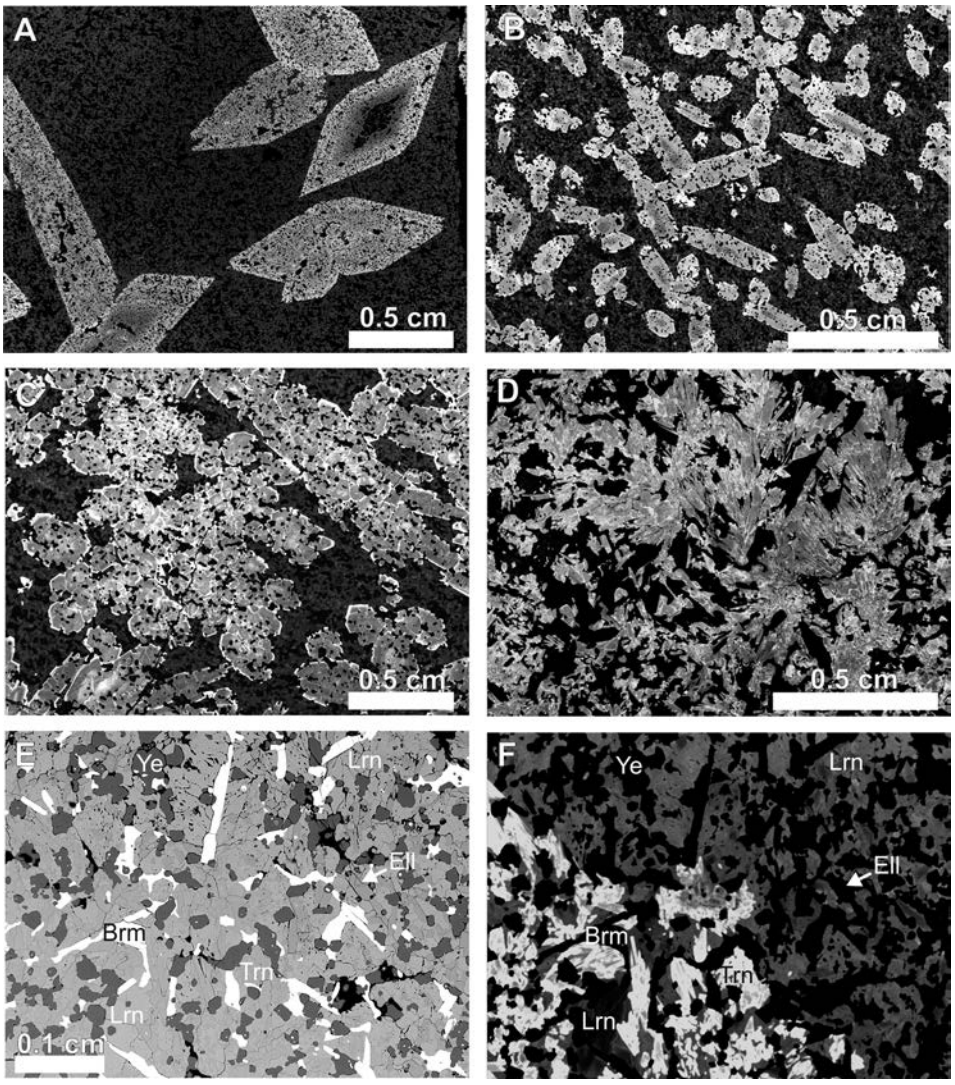

Fig. 6. Morphology of ternesite metacrysts (lighter) in cathodoluminescence (**A**-**D**, **F**) and BSE (**E**) images: **A** Jabel Harmun, **B** West Har Parsa, **C** Jabel Harmun (specimen shown in Fig. 4D); **D**-**F** Nabi Musa: **D** – spherulites of ternesite; **E**, **F** replacement front of fluorellestadite by ternesite. Lrn – larnite, Ye – ye'elimite, Brm – brownmillerite, Ell- fluorellestadite, Mgf – magnesioferrite, Trn – ternesite.

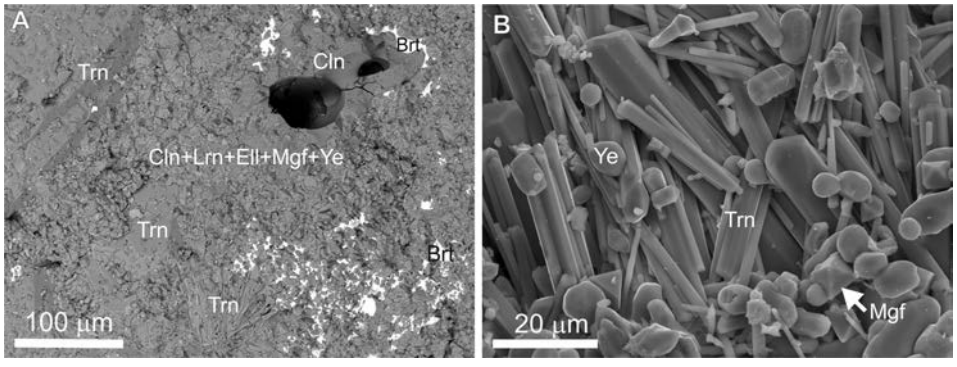

Fig. 7. **A** Fragment of larnite 'pebble' rich in calciolangbeinite and barite with cavities after gaseous inclusions in calciolangbeinite; **B** ternesite crystals in cavity with dissolved calciolangbeinite. Lrn – larnite, Ye – ye'elimite, Brt – barite, Ell- fluorellestadite, Mgf – magnesioferrite, Trn – ternesite, Cln – calciolangbeinite.

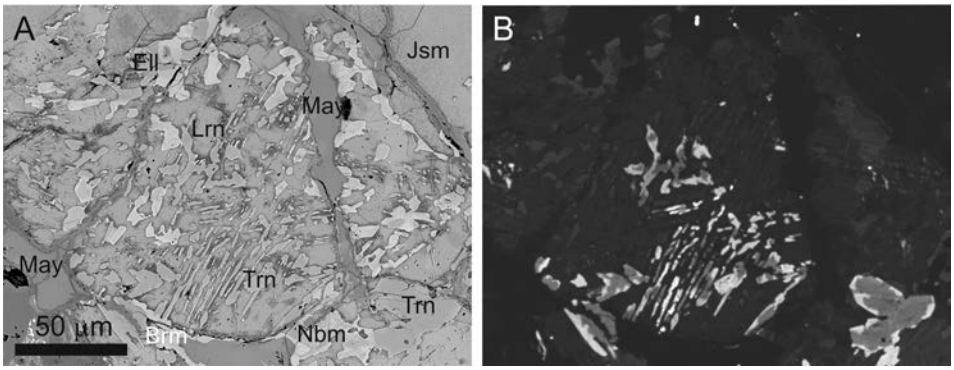

Fig. 8. Ternesite replacing flamite in decomposition products of the flamite–larnite solid solution: **A** BSE image, **B** cathodoluminescence image. Lrn – larnite, May – fluormayenite–fluorkyuygenite, Jsm – jasmundite, Ell- fluorellestadite, Brm – brownmillerite, Trn – ternesite, Nbm – nabimusaite.

Raman spectra and single-crystal data were also obtained for two P-bearing ternesite crystals: (1) high-P ternesite from Nabi Musa (specimen NM1) with a P_2O_5 content of 11.2 wt.% and the simplified formula $Ca_5[(Si_{0.8}P_{0.2})O_4]_2[(S_{0.6}P_{0.4})O_4]$ (Table 4), and (2) low-P ternesite from Jabel Harmun (IS93) with the simplified formula $Ca_5[(Si_{0.9}P_{0.1})O_4]_2[(S_{0.8}P_{0.2})O_4]$ (Table 3).

The Raman spectra of silicocarnotite show the following bands (cm^{-1}): 1085, 1056, 1014 [$\nu_3(PO_4) + \nu_3(SiO_4)$], 1004 $\nu_1(SO_4)$, 957 $\nu_1(PO_4)$, 850 $\nu_1(SiO_4)$, 640 $\nu_4(PO_4)$, 584 $\nu_4(PO_4) + (SiO_4)$, 557 $\nu_4(SiO_4)$, 474 $\nu_2(PO_4)$, 397 $\nu_2(SiO_4)$, 302, 234 ν(Ca-O) (Frost *et al*., 2007; Frost *et al*., 2011; Jastrzębski *et al*., 2011). The strongest bands may be assigned to vibrations of (SiO_4) and (PO_4) tetrahedra. The ratio of the ν_1 band vibration intensities $(SO_4):PO_4):(SiO_4)$ is a good diagnostic property for minerals of the ternesite–silicocarnotite solid solution series (Fig. 9). The ratios $\nu_1(SO_4):(PO_4):(SiO_4)$ for the three examples are the following: IS93, 0.3 P *pfu* ≈ 2:1.5:1; NM1, 0.8 P *pfu* ≈ 2:1:1.5; YV-415, 1.8 P *pfu* ≈ 1:8:2.

Raman maps of rankinite–silicocarnotite microsymplectite for the spectral range of the main bands of silicocarnotite, rankinite and kilchoanite (low-temperature dimorph of rankinite) confirm the diagnosis of silicocarnotite and rankinite (Fig. 10).

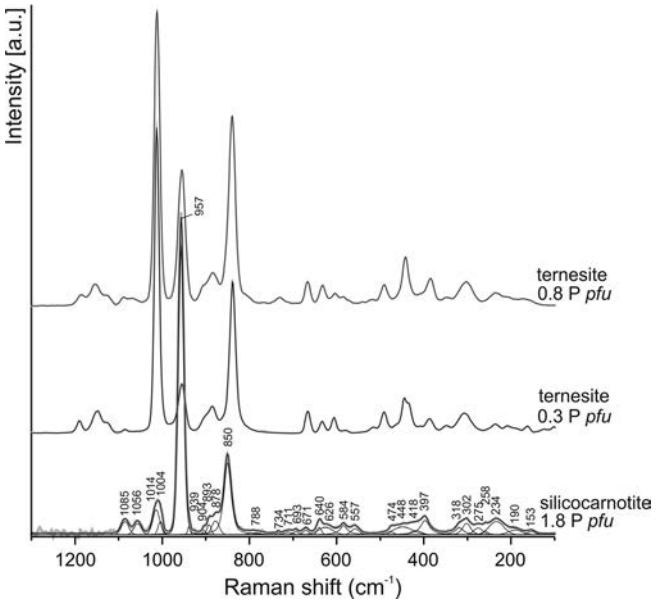

Fig. 9. Raman spectra of silicocarnotite and ternesite with different P_2O_5 contents.

Crystal structure of silicocarnotite and ternesite

The structure of synthetic S^{6+}+Si^{4+} was first solved by Dickens & Brown (1971). A few years later, the structure of synthetic $Ca_5(SiO_4)_2SO_4$ was described by Brotherton *et al*. (1974). Like their synthetic analogues, the minerals silicocarnotite and ternesite are isostructural. The details of single-crystal X-ray data collection and structure refinement of silicocarnotite (YV-415), high-P ternesite (NM1) and low-P ternesite (IS93) are summarised in Table 5. Atomic coordinates and equivalent isotropic atomic displacement parameters are listed in Table 6a–c. Selected interatomic distances are given in Table 7. Anisotropic displacement parameters for all three samples are listed in Table S3a–c (supplementary material).

The structures of silicocarnotite and ternesite exhibit two types of isolated tetrahedra ($T1O_4$ and $T2O_4$) connected via Ca ions. Figure 11 shows the structure of silicocarnotite projected along the **a** and **c** directions.

The $T1O_4$ tetrahedron is located on the mirror plane, and the *T*1 site is coordinated by O1, O2, and two O3 atoms. The *T*2 site is coordinated by O4, O5, O6, and O7.

In silicocarnotite (YV-415) the average *T*1–O distance is 1.55 Å (Table 7) and therefore the *T*1 site was refined as pure P. The $T2O_4$ tetrahedron shows a slightly larger average bond length of *ca*. 1.58 Å (Table 7). This indicates a mixed occupation of *T*2 by P and Si atoms. To maintain

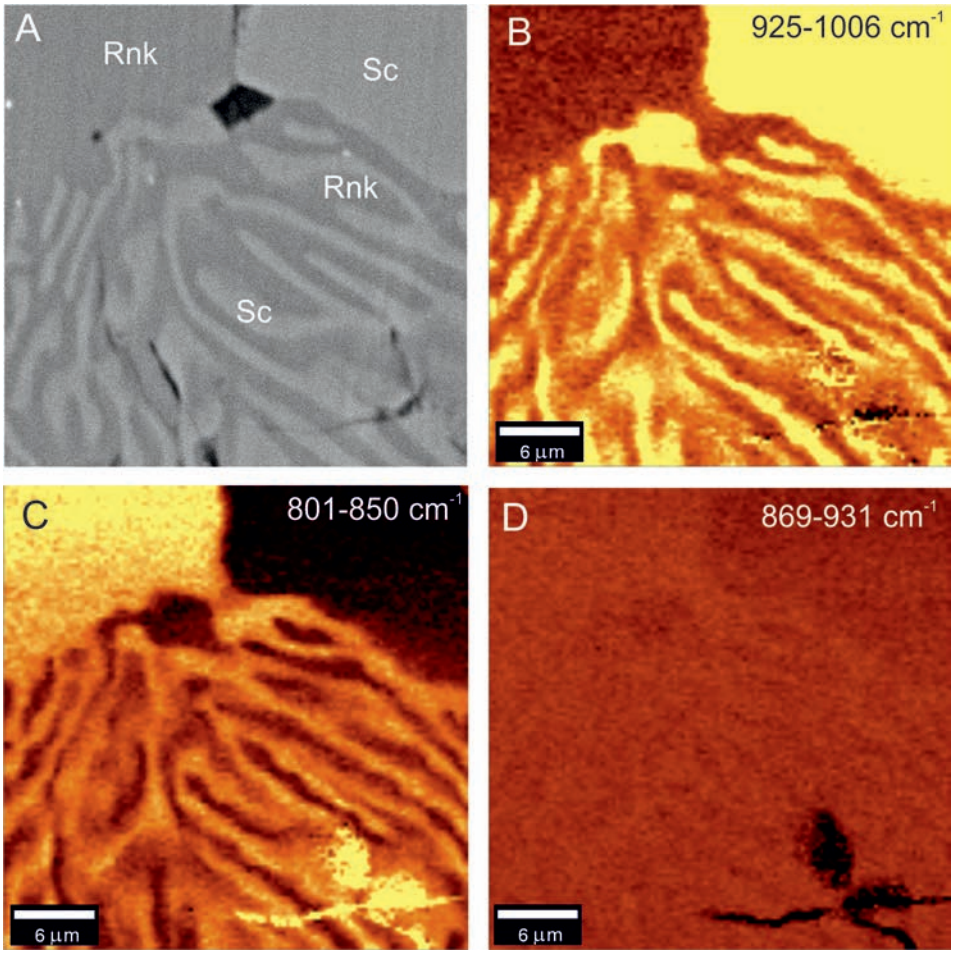

Fig. 10. Raman maps of silicocarnotite–rankinite symplectites: **A** BSE image, **B** range of main vibration, 925–1006 cm^{-1}, of silicocarnotite (Sc), **C** 801–931 cm^{-1}–rankinite (Rnk), **D** 869–931 cm^{-1}–kilchoanite.

charge balance, occupancy of 50 % P and 50 % Si is required at the *T*2 site. Considering the similar X-ray scattering factors of P and Si, the tetrahedral *T*2 site was modelled using fixed site occupancy factors. This is also in agreement with the model proposed by Dickens & Brown (1971) for synthetic $Ca_5(PO_4)_2SiO_4$.

In pure (idealised) ternesite $Ca_5(SiO_4)_2SO_4$, the *T*1 site is fully occupied by S^{6+} atoms, and the *T*2 site by Si atoms, with average bond lengths *T*1–O = 1.47 Å and *T*2–O = 1.64 Å (Irran *et al*., 1997). In low-P ternesite, $Ca_5[(Si_{0.9}P_{0.1})O_4]_2[(S_{0.8}P_{0.2})O_4]$, the average *T*–O bond lengths are 1.48 Å and 1.63 Å for *T*1 and *T*2, respectively (Table 7, IS93). The differences in average *T*–O bond lengths indicate the effect of the substitution $S^{6+}+Si^{4+}\rightarrow 2\ P^{5+}$, $T1O_4$ becoming larger and $T2O_4$ smaller. In P-rich ternesite, $Ca_5[(Si_{0.8}P_{0.2})O_4]_2[(S_{0.6}P_{0.4})O_4]$, the change in the average bond lengths is even more pronounced, with 1.49 Å in $T1O_4$ and 1.62 Å in $T2O_4$ (Table 7, NM1). This substitution mechanism may be regarded as the main reason for the increase of the unit-cell parameters in ternesite.

All three Ca sites in silicocarnotite may be described as seven-coordinated (Table 7). Bond lengths between calcium and oxygen atoms range between 2.395(2) and 2.624(4) Å (Table 8). The coordination of Ca1, however, requires a detailed discussion.

The neighbouring atoms of Ca1 include oxygen atoms of five tetrahedra: $2 \times T2O_4$ (O6 and O7); $2 \times T2O_4$ (O6) and $T1O_4$ (O2) (Fig. 12). Dickens & Brown (1971) have described Ca1 as eightfold coordinated with an additional Ca–O bond towards O2' of approximately 2.9 Å. Moreover, these authors report the highest residual electron density close to Ca1. This was interpreted as an artefact of V_2O_5 impurities in the crystal (Dickens & Brown, 1971). A residual electron density of 5.8 e^- at a distance of 0.35 Å from Ca1 has been observed in the difference Fourier map for sample YV-415, after refinement of the known structure model. The residual density has been interpreted as a split position of the Ca1 atoms (split into Ca1 and Ca1a, Fig. 11). The Ca1a site is shifted on the mirror plane towards O1, into the empty space between two *T*1 sites (Fig. 12).

The O1 atom bonds to *T*1 and twice to Ca2 and has a rather low bond-valence sum (1.8 *vu*). Moreover, O1 shows a significantly larger temperature factor (U_{eq} =

Table 5. Details of X-ray data collection and structure refinement of Silicocarnotite, P-rich ternesite and P-poor ternesite.

Crystal data	silicocarnotite	P-high ternesite	P-low ternesite
Unit cell dimensions (Å)	$a = 6.72230(1)$ $b = 15.4481(2)$ $c = 10.0847(2)$	$a = 6.8009(2)$ $b = 15.3625(3)$ $c = 10.1543(2)$	$a = 6.8428(1)$ $b = 15.3921(2)$ $c = 10.1836(1)$
Space group	*Pnma*	*Pnma*	*Pnma*
Volume (Å^3)	1047.37(2)	1060.91(4)	1072.59(2)
Z	4	4	4
Chemical formula	$Ca_5[(Si_{0.5}P_{0.5})O_4)]_2(PO_4)$	$Ca_5[(Si_{0.8}P_{0.2})O_4]_2[(S_{0.6}P_{0.4})O_4]$	$Ca_5[(Si_{0.9}P_{0.1})O_4]_2[(S_{0.8}P_{0.2})O_4]$
Intensity Measurement			
Crystal shape	prism	prism	prism
Crystal size (mm)	0.028 × 0.018 × 0.015	0.080× 0.030 × 0.025	0.110× 0.060 × 0.050
Diffractometer	SuperNova	SuperNova	Bruker APEX II SMART
X-ray radiation	Mo$K\alpha$	Mo$K\alpha$	Mo$K\alpha$
X-ray power	50 kV 30 mA	50 kV 30 mA	50 kV 30 mA
Monochromator	Graphite	Graphite	Graphite
Temperature	293(2)	293(2)	293(2)
Detector to sample distance	5.95 cm	5.95 cm	4.95 cm
Measurement method	Phi and Omega scans	Phi and Omega scans	Phi and Omega scans
Time per frame	60 s	60 s	10s
Index ranges	$-9 \le h \le 8$ $-22 \le k \le 21$ $-13 \le l \le 14$	$-9 \le h \le 9$ $-19 \le k \le 21$ $-14 \le l \le 14$	$-9 \le h \le 9$ $-21 \le k \le 21$ $-14 \le l \le 14$
No. of measured reflections	15739	8478	27077
No. of unique reflections	1657	1645	1698
No. of observed reflections ($I > 2\sigma$ (I))	1516	1460	1569
Refinement of the structure			
No. of parameters used in refinement	101	97	98
Rint	0.0290	0.0345	0.0321
Rσ	0.0139	0.0242	0.0122
R1, $I>2\sigma(I)$	0.0147	0.0227	0.0181
R1 all Data	0.0174	0.0279	0.0206
wR2 on (F2)	0.0401	0.0597	0.0514
GooF	1.076	1.077	1.079
$\Delta\rho$ min (-e. Å^{-3})	–0.393	–0.49 close to *T*2	−0.60 close to *T*1
$\Delta\rho$ max (e. Å^{-3})	0.074	0.55 close to Ca1	0.47 close to *T*1

0.0102(2) Å^2) as compared to the other O sites, and the longest axis of the displacement ellipsoid points towards Ca1a. In addition, the bond-valence sum of Ca1 (1.86 *vu*) is slightly below the expected value of 2. Based on these observations, an interaction between Ca1/Ca1a and O1 is presumable. The same phenomenon, to a smaller degree, has been observed in high-P ternesite (NM1) but not in low-P ternesite. Thus, splitting of the Ca1site depends on the cation at the *T*1 position. With S^{6+} in the tetrahedral site, O1 is not under-bonded and does not interact with Ca1.

The crystal structure of silicocarnotite is closely related to the apatite structure. This relation has been discussed by Keppler (1968); Dickens & Brown (1971), and Gomes *et al*. (2011). In addition, a structural relation to glaserite (aphthitalite) $K_3Na(SO_4)_2$ has also been reported (Dickens & Brown, 1971). Along with $Ca_{15}(SiO_4)_6(PO_4)_2$ (flamite-like) and nagelschmidtite $Ca_7(SiO_4)_2(PO_4)_2$ (Widmer *et al*., 2015), silicocarnotite is the third intermediate phase in the system $Ca_2(SiO_4)$–$Ca_3(PO_4)_2$.

The structure of silicocarnotite may be derived from the orthohexagonal polymorph of dicalcium silicate ($\alpha'_{(H)}$-Ca_2SiO_4). Modules of $\alpha'_{(H)}$-$Ca_2(Si,P)O_4$ with a stretched **c** axis are inter-sliced by modules of $CaPO_4$ composition in the silicocarnotite structure. This leads to an alternation of the $[Ca_4(SiO_4)(PO_4)]^+$ and $[Ca(PO_4)]^-$ modules along the **a** axis in the 1:1 ratio (Fig. 13).

Discussion

The occurrence of large ternesite porphyroblasts in a fine-grained larnite matrix requires reconsideration of the hitherto suggested two-stage models for the formation of the pyrometamorphic rocks of the Hatrurim Complex. Larnite rocks of the Hatrurim Complex are considered as natural analogues of Portland-cement clinkers. With the high content of ye'elimite in these rocks, they have been suggested to be prototypes of sulphate-aluminate ''green'' cements (Sokol *et al*., 2014). The synthetic analogue of ternesite forms as an intermediate phase in the production process of sulphate-aluminate cement at 900°C and remains stable up to 1200–1280°C (Beretka *et al*., 1993).

Table 6. Fractional atomic coordinates and displacement parameters (U_{eq}, in Å^2) for silicocarnotite (a), P-rich ternesite (b) and P-poor ternesite (c).

Site	Atom	*x*	*y*	*z*	U_{eq}	Occ.
a. Silicocarnotite						
Ca1	Ca	0.0417(2)	1/4	0.1857(3)	0.0078(3)	0.923(16)
Ca1a	Ca	0.021(2)	1/4	0.154(3)	0.0078(3)	0.077(16)
Ca2	Ca	0.16883(4)	0.893218(16)	0.16472(2)	0.00680(6)	1
Ca3	Ca	0.36794(4)	0.092085(15)	0.06481(2)	0.00576(6)	1
*T*1	P	0.02769(7)	1/4	0.57767(4)	0.00560(9)	1
*T*2	P	0.35129(5)	0.07217(2)	0.36869(3)	0.00372(7)	0.50
	Si	0.35129(5)	0.07217(2)	0.36869(3)	0.00372(7)	0.50
O1	O	0.2570(2)	1/4	0.57845(13)	0.0102(2)	1
O2	O	0.93467(19)	1/4	0.43596(13)	0.0077(2)	1
O3	O	0.95784(14)	0.16567(6)	0.64643(9)	0.00949(18)	1
O4	O	0.40802(13)	0.99435(6)	0.27350(9)	0.00717(17)	1
O5	O	0.18801(13)	0.04385(5)	0.47338(9)	0.00611(16)	1
O6	O	0.27472(13)	0.14889(6)	0.27683(9)	0.00680(16)	1
O7	O	0.52933(13)	0.11055(6)	0.45412(9)	0.00774(17)	1
b. P-rich ternesite						
Ca1	Ca	0.04659(11)	1/4	0.18869(12)	0.0101(2)	0.987(4)
Ca1a	Ca	0.012(9)	1/4	0.139(9)	0.0101(2)	0.013(4)
Ca2	Ca	0.15146(6)	0.89992(2)	0.16053(3)	0.00891(9)	1
Ca3	Ca	0.36390(5)	0.08829(2)	0.06588(3)	0.00697(9)	1
*T*1	S	0.02073(11)	1/4	0.58502(6)	0.00912(14)	0.60
	P	0.02073(11)	1/4	0.58502(6)	0.00912(14)	0.40
*T*2	Si	0.34773(7)	0.07394(3)	0.36703(4)	0.00472(11)	0.80
	P	0.34773(7)	0.07394(3)	0.36703(4)	0.00472(11)	0.20
O1	O	0.2390(4)	1/4	0.5956(2)	0.0207(5)	1
O2	O	0.9499(3)	1/4	0.44491(16)	0.0091(3)	1
O3	O	0.9435(2)	0.16905(8)	0.64801(12)	0.0165(3)	1
O4	O	0.39408(19)	0.99203(7)	0.27099(11)	0.0079(2)	1
O5	O	0.18313(19)	0.04861(7)	0.47501(11)	0.0069(2)	1
O6	O	0.28287(19)	0.15260(7)	0.27096(11)	0.0072(2)	1
O7	O	0.5308(2)	0.11030(8)	0.45415(11)	0.0088(3)	1
c. P-poor ternesite						
Ca1	Ca	0.04902(6)	1/4	0.18964(4)	0.01335(9)	1
Ca2	Ca	0.14481(4)	0.902011(19)	0.15904(3)	0.01270(8)	1
Ca3	Ca	0.36274(4)	0.086863(18)	0.06590(3)	0.01060(8)	1
T1	S	0.01824(9)	1/4	0.58772(5)	0.01533(11)	1
T2	Si	0.34654(5)	0.07426(2)	0.36612(3)	0.00708(9)	1
O1	O	0.2326(3)	1/4	0.5997(2)	0.0306(4)	1
O2	O	0.9525(2)	1/4	0.44870(14)	0.0164(3)	1
O3	O	0.9392(2)	0.17036(7)	0.64925(11)	0.0276(3)	1
O4	O	0.38846(15)	0.99125(7)	0.27019(10)	0.0128(2)	1
O5	O	0.18134(14)	0.05052(6)	0.47508(9)	0.01002(18)	1
O6	O	0.28660(14)	0.15354(6)	0.26908(9)	0.01103(19)	1
O7	O	0.53146(15)	0.10929(7)	0.45352(10)	0.0142(2)	1

Ternesite from altered xenoliths in Eifel volcanites (Germany) formed at 1000–1300°C (Irran *et al*., 1997). These observations indicate that ternesite from the Hatrurim Complex is a high-temperature mineral. Large ternesite metacrysts formed in a fine-grained larnite–ye'elimite–fluorellestadite matrix (Figs 5A, B; 6A, B). The formation of such idiomorphic, large ternesite porphyroblasts/metacrysts is only possible in the presence of an interstitial fluid phase. The mechanism of similar metacryst formation in a solid substrate is known; when a capillary film of fluid on the surface of a metacryst dissolves minerals of the substrate, growth of a metacryst takes place simultaneously (*e.g*. Beus, 1962; Carmichael, 1969).

The most probable liquid phases responsible for the formation of ternesite porphyroblasts are not in equilibrium with the primary ''clinker'' minerals' (fluorellestadite and larnite) sulphate-bearing melts. On fresh surfaces of the specimens examined, hydrosoluble minerals such as calciolangbeinite, aphthitalite, sylvite *etc*. have been noted (Fig. 7; Galuskina *et al*., 2014a). These minerals may be regarded as the crystallized remains of sulphate-bearing (+halogens) melts.

Silicocarnotite with near-end-member composition in gehlenitic rocks underwent a similar alteration as described for ternesite above. Porous grains of silicocarnotite probably replaced high-phosphorous flamite. The presence of reaction margins composed of

Table 7. Selected interatomic distances for silicocarnotite and ternesite.

Site 1	Site 2	Silicocarnotite YV-415	P-rich ternesite NM1	P-poor ternesite IS93
Ca1	O2	2.624(3)	2.684(2)	2.7196(16)
	O2	2.9127(14)	3.0597(19)	
	O6 2x	2.395(3)	2.3492(15)	2.3456(10)
	O6 2x	2.4094(12)	2.3714(13)	2.3676(10)
	O7 2 x	2.576(2)	2.5926(14)	2.6135(11)
Ca1a	O1	2.94(3)	3.02(9)	
	O2	2.90(2)	3.10(7)	
	O2	2.927(11)	3.13(10)	
	O6 2x	2.380(8)	2.35(4)	
	O6 2x	2.63(2)	2.35(4)	
	O7 2x	2.414(12)	2.35(4)	
Ca2	O1	2.4291(6)	2.5089(9)	2.5580(8)
	O3	2.2759(9)	2.3064(13)	2.3200(12)
	O3	2.6760(10)	*2.9542(17)*	*3.0586(16)*
	O4	2.4297(9)	2.3558(13)	2.3416(10)
	O4	2.4960(9)	2.4461(13)	2.4388(11)
	O5	2.3654(9)	2.3323(12)	2.3364(10)
	O7	2.5078(9)	2.4399(13)	2.4219(11)
Ca3	O2	2.4804(3)	2.5545(6)	2.5893(5)
	O3	2.4891(9)	2.5592(13)	2.5933(12)
	O4	2.6041(9)	2.5626(12)	2.5544(10)
	O5	2.3096(9)	2.2929(13)	2.2891(10)
	O5	2.3241(9)	2.3188(11)	2.3277(10)
	O6	2.3947(9)	2.3700(12)	2.3676(10)
	O7	2.3021(9)	2.2993(14)	2.3015(11)
*T*1	O1	1.5415(14)	1.488(2)	1.472(2)
	O2	1.5600(13)	1.5022(18)	1.4855(15)
	O3 2x	1.5487(9)	1.4938(13)	1.4792(12)
*T*2	O4	1.5850(9)	1.6229(12)	1.6337(10)
	O5	1.5846(9)	1.6145(13)	1.6256(10)
	O6	1.5898(9)	1.6145(12)	1.6230(10)
	O7	1.5895(9)	1.6264(13)	1.6383(11)

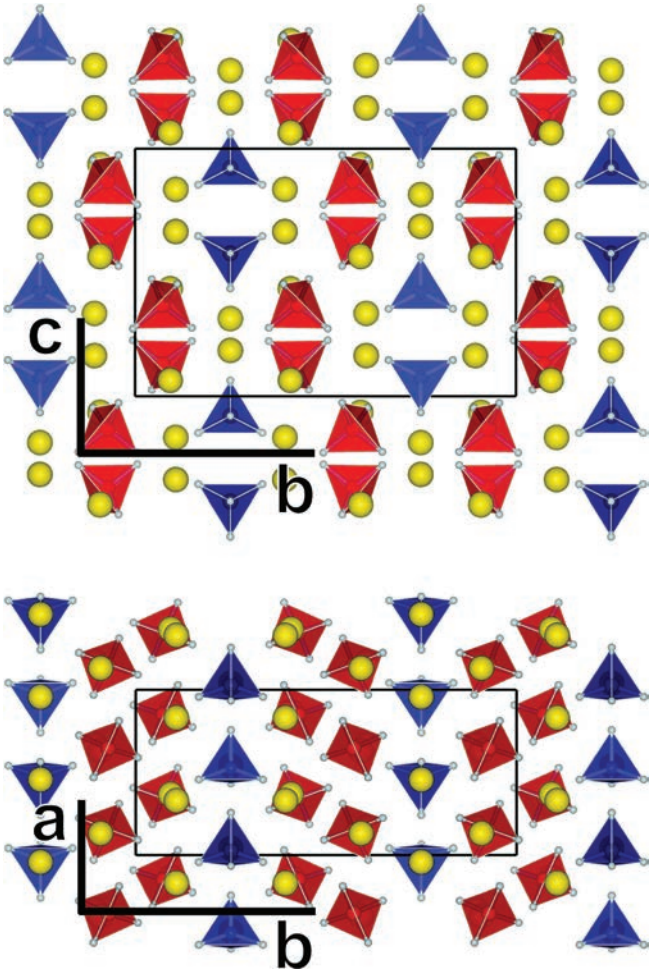

Fig. 11. The crystal structure of silicocarnotite seen along the **a** and **c** directions. The structure contains two tetrahedral sites *T*1 (blue) and *T*2 (red). *T*1 is a pure PO_4 tetrahedron whereas *T*2 is occupied by 50 % Si and 50 % P. Calcium atoms are drawn as yellow spheres.

silicocarnotite–rankinite symplectites explicitly show the non-equilibrium character of the melt-driven alteration process (Fig. 1B).

Silicocarnotite found as a minor constituent in the holotype specimen YV-415 replaces primary fluorapatite. The association of silicocarnotite with parawollastonite, which is stable at sanidinite-facies conditions at temperatures higher than 1100°C (Vapnik *et al*., 2015), may indicate that the temperature of crystallization of "pure" silicocarnotite is higher than the temperature of crystallization of "pure" ternesite.

The P_2O_5 content in the newly formed minerals of the ternesite–silicocarnotite series correlates with the composition of the associated ellestadite–apatite grains, belonging to the early clinker paragenesis. The dependence may be described by the equation $^{Sc\text{-}Trn}P_2O_5 = {}^{ellestadite}0.9\ P_2O_5 - 5.7$ (Fig. 14). However, flamite (P_2O_5 up to 17 %) and larnite (P_2O_5 up to 4 %) are also sources of P for minerals of the silicocarnotite–ternesite solid solution. In the case of larnite, there is no evidence of correlation between its composition and that of newly formed minerals of the ternesite–silicocarnotite series (Fig. S1; Tables S4 and S5). For a correlation between the pseudomorphs after flamite and flamite, we do not have sufficient data.

Side-products of the combustion processes during the pyrometamorphism, such as gas, melt, and fluid, react with previously formed minerals. These secondary, high-temperature alterations allow the formation of a significantly greater diversity of pyrometamorphic minerals than in the common "dry clinker" association. Besides minerals of the silicocarnotite–ternesite series, nabimusaite (Galuskin *et al*., 2015b) is a product of melt reaction with "clinker phase". Oldhamite, jasmundite and dzierżanowskite (Galuskin *et al*., 2013c; Galuskina *et al*., 2014b) as well as fluorkyuygenite after fluormayenite (Galuskin *et al*., 2015a), are alteration products formed by interaction with sulphur-bearing and H_2O-bearing gases with minerals of the clinker association.

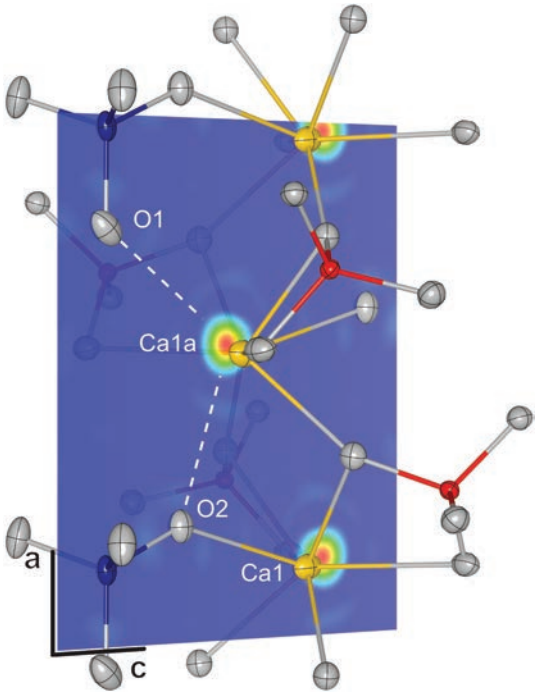

Fig. 12. A perspective close up of the surroundings of the Ca1 site in silicocarnotite. *T*1 is blue, *T*2 red, Ca-atoms yellow and O shown as grey ellipsoids. In the mirror plane perpendicular to [010] the difference Fourier map after refinement of the known structure model is shown. Residual electron density of ≈ 5.8 e^- indicates a splitting of the Ca1 site and interaction with the adjacent O1 and potentially O2 sites. The coordination of Ca1/Ca1a is best described by seven main bonds (O6, O6', O6'', O7, O7' O7'', O2) and two weak bonds O2' and O1.

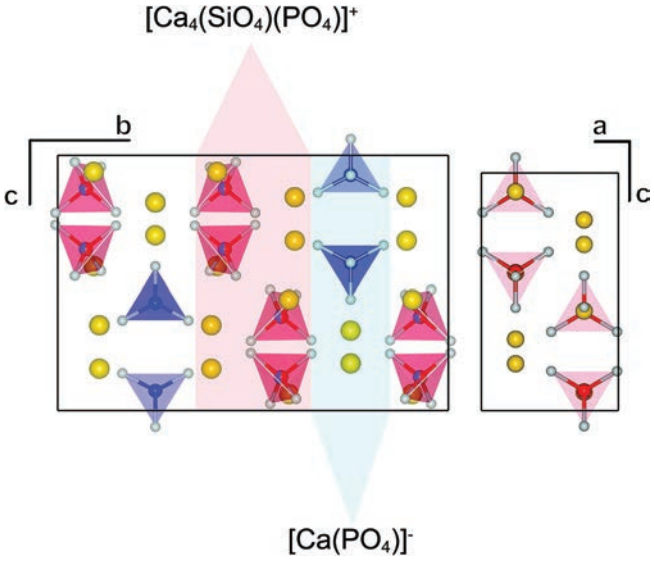

Fig. 13. Comparison of the structures of silicocarnotite (left) and $\alpha'_{(H)}$-C_2S (right). The Ca atoms are shown as yellow spheres, PO_4 tetrahedra are blue, SiO_4 and mixed tetrahedra are red. The structure of silicocarnotite may be seen as a 1:1 alternation of streched $\alpha'_{(H)}$-C_2S modules with a P/Si ratio of 1:1, inter-sliced by $Ca(PO_4)^-$ modules.

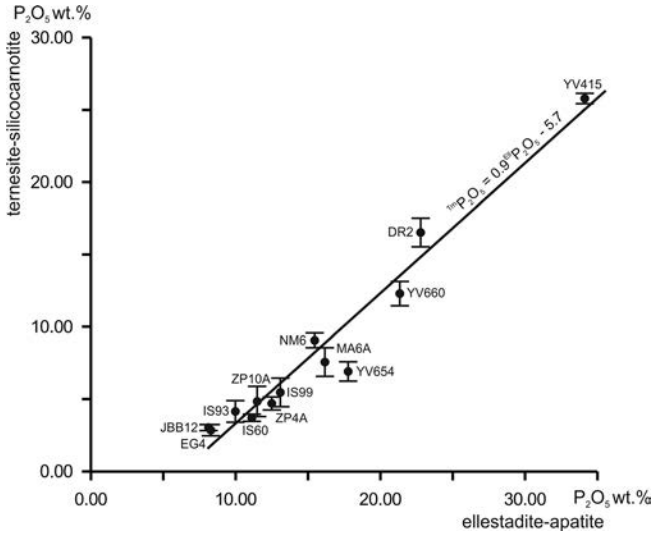

Fig. 14. Correlation between the P_2O_5 content of newly formed silicocarnotite–ternesite and of primary ellestadite–apatite.

Acknowledgements: We express our thanks to our friend and teacher Thomas Armbruster for his cooperation in our projects and a great help in solving the mineral structures. The authors thank two anonymous reviewers for their careful review that improved the early version of the manuscript. Eva Wadoski-Romeijn helped with the English. The work was partly supported by the National Science Centre (NCN) of Poland, grant no. DEC-2012/05/B/ST10/00514.

References

Bentor, Y. (1960): Israel. *in* "Lexique stratigraphique international, Asie", Centre National de la Recherche Scientifique, Paris, France, Vol. 3, part 10.2, 80 p.

Beretka, J., de Vito, B., Santoro, L., Sherman, N., Valenti, G.L. (1993): Hydraulic behaviour of calcium sulfoaluminate-based cements derived from industrial process wastes. *Cem. Concr. Res.*, **23**, 1205–1214.

Beus, A.A. (1962): About mechanism of REE-minerals idiomorphic crystals formation in replacement processes. *Proc. IMGRE*, **1061**(7), 61–64.

Britvin, S.N., Murashko, M.N., Vapnik, Y., Polekhovsky, Yu. S., Krivovichev, S.V. (2015): Earth's phosphides in levant and insights into the source of Archean prebiotic phosphorus. *Sci. Rep.*, **5**, 8355. doi:10.1038/srep08355

Brotherton, P.D., Epstein, J.M., Pryce, M.W., White, A.H. (1974): Crystal structure of "calcium sulphosilicate", $Ca_5(SiO_4)_2SO_4$. *Austral. J. Chem.*, **27**, 657–660.

Carmichael, D.M. (1969): On the mechanism of prograde metamorphic reactions in quartz-bearing pelitic rocks. *Contrib. Mineral. Petrol.*, **20**, 244–267.

Carnot, A. & Richard, A. (1883): Silicophosphate de chaux cristallisé produit dans la déphosphoration des fontes. *C. R. Hebd. Séances Acad. Sci. Paris*, **97**, 316–320.

Dickens, B. & Brown, W.E. (1971): The crystal structure of $Ca_5(PO_4)_2SiO_4$ (silico-carnotite). *Tschermaks Mineral. Petrogr. Mitt.*, **16**, 1–27.

Eytier, J.R., Eytier, Ch., Favreau, G., Devouard, B., Vigier, J. (2004): Minéraux de pyrométamorphisme de Lapanouse de Sévérac (Aveyron). *Le Cahier des Micromonteurs*, **85**, 3–58.

Friedel, C. & Cumenge, E. (1899): Sur un nouveau minerai d'urane, la carnotite. *C. R. Hebd. Séances Acad. Sci. Paris*, **128**, 532–534.

Frost, R.L., Weier, M.L., Mills, S. J. (2007): A vibrational spectroscopic study of perhamite, an unusual silico-phosphate. *Spectrochim. Acta, Part A*, **67**, 604–610.

Frost, R.L., Palmer, S.J., Xi, Y. (2011): A vibrational spectroscopic study of the mineral hinsdalite $(Pb,Sr)Al_3(PO_4)(SO_4)(OH)_6$. *J. Mol. Struct.*, **1001**, 43–48.

Galuskin, E.V., Kusz, J., Armbruster, T., Galuskina, I.O., Marzec, K., Vapnik, Ye., Murashko, M. (2013a): Vorlanite, $(CaU^{6+})O_4$, from Jabel Harmun, Palestinian Autonomy, Israel. *Am. Mineral.*, **98**, 1938–1942.

Galuskin, E., Galuskina, I., Lazic, B., Vapnik, Ye. (2013b): Rock-forming P-bearing ternesite from pyrometamorphic rocks of the Hatrurim formation, Israel. *Mineralogia - Special Papers*, **41**, 40.

Galuskin, E.V., Galuskina, I.O., Vapnik, Y., Murashko, M., Prusik, K., Dzierżanowski, P. (2013c): Oldhamite CaS and potentially new mineral $CaCu_2S_2$ from pyrometamorphic rock of the Hatrurim formation. Goldschmidt2013 conference abstracts. *Mineral. Mag*, **77**, 1134.

Galuskin, E.V., Galuskina, I.O., Kusz, J., Armbruster, T., Marzec, K.M., Dzierżanowski, P., Murashko, M. (2014): Vapnikite Ca_3UO_6–a new double-perovskite mineral from pyrometamorphic larnite rocks of the Jabel Harmun, Palestinian Autonomy, Israel. *Mineral. Mag.*, **78**, 571–581.

Galuskin, E.V., Gfeller, F., Armbruster, T., Galuskina, I.O., Vapnik, Ye., Dulski, M., Murashko, M., Dzierżanowski, P., Sharygin, V.V., Krivovichev, S.V., Wirth, R. (2015a): Mayenite supergroup, Part III: Fluormayenite, $Ca_{12}Al_{14}O_{32}[_{\square 4}F_2]$, and fluorkyuygenite, $Ca_{12}Al_{14}O_{32}[(H_2O)_4F_2]$, two new minerals of mayenite supergroup from pyrometamorphic rock of hatrurim complex. *Eur. J. Mineral.*, **27**, 123–136.

Galuskin, E.V., Gfeller, F., Armbruster, T., Galuskina, I.O., Vapnik, Ye., Murashko, M., Włodyka, R., Dzierżanowski, P. (2015b): New minerals with modular structure derived from hatrurite from the pyrometamorphic Hatrurim Complex, Part I: Nabimusaite, $KCa_{12}(SiO_4)_4(SO_4)_2O_2F$, from larnite rock of the Jabel Harmun, Palestinian Autonomy, Israel. *Mineral. Mag.*, (in press).

Galuskin, E.V., Gfeller, F., Galuskina, I.O., Pakhomova, A., Armbruster, T., Vapnik, Y., Włodyka, R., Dzierżanowski, P., Murashko, M. (2015c): New minerals with modular structure derived from hatrurite from the pyrometamorphic Hatrurim Complex, Part II: Zadovite, $BaCa_6[(SiO_4)(PO_4)](PO_4)_2F$, and aradite, $BaCa_6[(SiO_4)(VO_4)](VO_4)_2F$, from paralavas of the Hatrurim Basin, Negev Desert, Israel. *Mineral. Mag.*, (in press).

Galuskin, E.V., Gfeller, F., Galuskina, I.O., Armbruster, T., Bailau, R., Sharygin, V.V. (2015d): Mayenite supergroup, part I: recommended nomenclature. *Eur. J. Mineral.*, **27**, 99–111.

Galuskina, I.O., Vapnik, Y., Prusik, K., Dzierżanowski, P., Murashko, M., Galuskin, E.V. (2013): Gurimite, IMA 2013–032. CNMNC Newsletter No. 16, August 2013, page 2708. *Mineral. Mag.*, **77**, 2695–2709.

Galuskina, I.O., Vapnik, Ye., Lazic, B., Armbruster, T., Murashko, M., Galuskin, E.V. (2014a): Harmunite $CaFe_2O_4$–a new mineral from the Jabel Harmun, West Bank, Palestinian Autonomy, Israel. *Am. Mineral.*, **99**, 965–975.

Galuskina, I.O., Galuskin, E.V., Pakhomova, A.S., Widmer, R., Armbruster, T., Lazic, B., Grew, E.S., Vapnik, Y., Dzierżanowski, P., Murashko, M. (2014b): Khesinite, IMA 2014–033. CNMNC Newsletter No. 21, 802. *Mineral. Mag.*, **78**, 797–804.

Galuskina, I.O., Galuskin, E.V., Prusik, K., Vapnik, Y., Jeżak, L., Murashko, M. (2014c): Dzierżanowskite, IMA 2014–032. CNMNC Newsletter No. 21, August 2014, page 802. *Mineral. Mag.*, **78,** 797–804.

Gatel, P., Žáček, V., Kruszewski, Ł., Devouard, B., Thiéry, V., Eytier, C., Eytier, J.-R., Favreau, G., Vigier, G., Stracher, G. B. (2015): Combustion mineralogy and petrology of oil-shale slags in Lapanouse, Sévérac-le-Château, Aveyron, France: Analogies with hydrocarbon fires. *in* ''Coal and peat fires: a global perspective'', G.B. Stracher, A. Prakash, and E.V. Sokol, ed. Elsevier, Amsterdam, Vol. **3**, 682–742.

Geller, Y.I., Burg, A., Halicz, L., Kolodny, Y. (2012): System closure during the combustion metamorphic'' Mottled Zone'' event, Israel. *Chem. Geol.*, **334**, 25–36.

Gfeller, F., Widmer, R., Krüger, B., Galuskin, E.V., Galuskina, I.O., Armbruster, T. (2015): The crystal structure of flamite and its relation to Ca_2SiO_4 polymorphs and nagelschmidtite. *Eur. J. Mineral.*, **27**, doi:10.1127/ejm/2015/0027-2476.

Gomes, S., Nedelec, J.-M., Jallot, E., Sheptyakov, D., Renaudin, G. (2011): Silicon location in silicate-substituted calcium phosphate ceramics determined by neutron diffraction. *Cryst. Growth Des.*, **11**, 4017–4026.

Gross, S. (1977): The mineralogy of the Hatrurim Formation, Israel. *Bull. - Geol. Surv. Isr.*, **70**, 1–80.

Gross. (1984): Occurrence of ye'elimite and ellestadite in an unusual cobble from the ''pseudo-conglomerate'' of the Hatrurim Basin. *Israel. Geol. Surv. Isr., Current Research*, **1983–84**, 1–4.

Gualtieri, A.F., Cavenati, C., Zanatto, I., Meloni, M., Elmi, G., Lassinantti Gualtieri, M. (2008): The transformation sequence of cement–asbestos slates up to 1200°C and safe recycling of the reaction product in stoneware tile mixtures. *J. Hazard. Mater.*, **152**, 563–570.

Irran, E., Tillmanns, E., Hentschel, G. (1997): Ternesite, $Ca_5(SiO_4)_2SO_4$, a new mineral from the Ettringer Bellerberg/Eifel, Germany. *Mineral. Petrol.*, **60**, 121–132.

Jastrzębski, W., Sitarz, M., Rokita, M., Bułat, K. (2011): Infrared spectroscopy of different phosphates structures. *Spectrochim. Acta A*, **79**, 722–727.

Keppler, U. (1968): S-Phase und Verbindung C5PS, $Ca_5(PO_4)_2SiO_4$. *Neues Jahrb. Mineral. Mh.*, **1968**(9), 320–330.

Kolodny, Y. & Gross, S. (1974): Thermal metamorphism by combustion of organic matter: isotopic and petrological evidence. *J. Geol.*, **82**, 489–506.

Kolodny, Y., Burg, A., Sneh, A. (2013): Comment on ''Combustion metamorphism in the Nabi Musa dome: new implications for a mud volcano origin of the Mottled Zone, Dead Sea area'', by E. Sokol, I. Novikov, S. Zateeva, Ye. Vapnik, R. Shagam and O. Kozmenko, Basin Research (2010), 22, 414–438. *Basin Res.*, **25**, 112–114.

Kolodny, Y., Burg, A., Geller, Y.I., Halicz, L., Zakon, Y. (2014): Veins in the combusted metamorphic rocks, Israel; weathering or a retrograde event. *Chem. Geol.*, **385**, 140–155.

Kraus, W. & Nolze, G. (1996): POWDER CELL – a program for the representation and manipulation of crystal structures and calculation of the resulting X-ray powder patterns. *J. Appl. Cryst.*, **29**, 301–303.

Kroll, V.A. (1911): Researches on the nature of the phosphates contained in basic slags derived from the Thomas-Gilchrist dephosphorisation process. *J. Iron Inst.*, **84**, 126–187.

Martínez, I.M., Velásquez, P., De Aza, P.N. (2012): The sub-system α-TCPss-Silicocarnotite within the binary system $Ca_3(PO_4)2$–Ca_2SiO_4. *J. Am. Ceram. Soc.*, **95**, 1112–1117.

Matthews, A. & Gross, S. (1980): Petrologic evolution of the Mottled Zone (Hatrurim) metamorphic complex of Israel. *Isr. J. Earth Sci.*, **29**, 93–106.

Murashko, M. N., Chukanov, N. V., Mukhanova, A. A., Vapnik, Ye., Britvin, S. N., Polekhovsky, Yu. S., Ivakin, Yu. D. (2011): Barioferrite $BaFe_{12}O_{19}$: A new mineral species of the magnetoplumbite group from the Haturim Formation in Israel. *Geol. Ore Depos.*, **7**, 558–563.

Novikov, I., Vapnik, Ye., Safonova, I. (2013): Mud volcano origin of the Mottled Zone, South Levant. *Geosci. Front*, **4**, 597–619.

Radev, L., Fernandes, M.H.V., Salvado, I.M., Kovacheva, D. (2009): Organic/Inorganic bioactive materials Part III: *in vitro* bioactivity of gelatin/silicocarnotite hybrids. *Cent. Eur. J. Chem.*, **7**, 721–730.

Riley, D.P. & Segnit, E.R. (1949): An optical and X-ray examination of the basic-slag mineral silicocarnotite. *Mineral. Mag.*, **28**, 496–504.

Roh, H.-S., Hur, S., Song, H.J., Park, I.J., Yim, D.K., Kim, D.-W., Hong, K.S. (2012): Luminescence properties of $Ca_3(PO_4)_2SiO_4$: Eu^{2+} green phosphor for near UV-based with LED. *Mater. Lett.*, **70**, 37–39.

Saalfeld, H. & Klaska, H.K. (1981): The crystal structure of 6 $Ca_2SiO_4 \cdot 1\ Ca_3(PO_4)_2$. *Z. Kristallogr.*, **155**, 65–73.

Sharygin, V.V., Lazic, B., Armbruster, T.M., Murashko, M.N., Wirth, R., Galuskina, I.O., Galuskin, E.V., Vapnik, Ye., Britvin, S.N., Logvinova, A.M. (2013): Shulamitite $Ca_3TiFe^{3+}AlO_8$—A new perovskite-related mineral from Hatrurim Basin, Israel. *Eur. J. Mineral.*, **25**, 97–111.

Sheldrick, G.M. (2008): A short history of SHELX. *Acta Crystallogr. A*, **64**, 112–122.

Sokol, E., Novikov, I., Zateeva, S., Vapnik, Ye., Shagam, R., Kozmenko, O. (2010): Combustion metamorphism in the Nabi Musa dome: New implications for a mud volcanic origin of the Mottled Zone, Dead Sea area. *Basin Res.*, **22**, 414–438.

Sokol, E.V., Kokh, S.N., Vapnik, Ye., Thiéry, V., Korzhova, S.A. (2014): Natural analogs of belite sulfoaluminate cement clinkers from Negev Desert, Israel. *Am. Mineral.*, **99**, 1471–1487.

Sokol, E.V., Seryotkin, Y.V., Kokh, S.N., Vapnik, Y., Nigmatulina, E.N., Goryainov, S.V., Belogub, E.V., Sharygin, V.V. (2015): Flamite, $(Ca,Na,K)_2(Si,P)O_4$, a new mineral from ultrahigh-temperature combustion metamorphic rocks, Hatrurim Basin, Negev Desert, Israel. *Mineral Mag.*, **79**, 583–596.

Sundberg, I. & Sillén, L.G. (1949): On the crystal structure of KUO_2VO_4 (synthetic anhydrous carnotite). *Ark. Kemi*, **1**, 337–351.

Trömmel, G. & Zaminer, C. (1959): Untersuchungen an den Kristallen der Thomas Schlacke. *Archiv für das Eisenhüttenwesen*, **30**, 205–209.

Vapnik, Y. & Novikov, I. (2013): Reply to Comment of Y. Kolodny, A. Burg, and A. Sneh on Combustion metamorphism in the Nabi Musa dome: new implications for a mud volcano origin of the Mottled Zone, Dead Sea area, by E. Sokol, I. Novikov, S. Zateeva, Ye. Vapnik, R. Shagam and O. Kozmenko, Basin Research (2010) 22, 414–438. *Basin Res.*, **25**, 115–120.

Vapnik, Y. & Vardi, J. (2013): Combustion metamorphic stone tools, Hatrurim basin, Israel. *in* "Coal and peat fires: a global perspective", G.B. Stracher, A. Prakash, and E.V. Sokol, eds. Elsevier, Amsterdam, Vol. **2**, 191–203.

Vapnik, Y., Sharygin, V.V., Sokol, E.V., Shagam, R. (2007): Paralavas in a combustion metamorphic complex: Hatrurim Basin, Israel. *Rev. Eng. Geol.*, **18**, 1–21.

Vapnik, Y., Galuskina, I., Palchik, V., Sokol, E.V., Galuskin, E., Lindsley-Griffin, N., Stracher, G.B. (2015): Stone-tool workshops of the Hatrurim Basin, Israel: mineralogy, geochemistry, and rock mechanics of lithic industrial materials. *in* "Coal and peat fires: a global perspective", G.B. Stracher, A. Prakash, and E.V. Sokol, ed. Elsevier, Amsterdam, Vol. **3**, 281–316.

Widmer, R., Gfeller, F., Armbruster, T. (2015): Structural and crystal chemical investigation of intermediate phases in the system Ca_2SiO_4–$Ca_3(PO_4)_2$–$CaNaPO_4$. *J. Am. Ceram. Soc.*, 1–10. doi: 10.1111/jace.13850.

Yu, H., Deng, D., Li, Y., Xu, S., Li, Y., Yu, C., Ding, Y., Lu, H., Yin, H., Nie, Q.L. (2013): Electronic structure and luminescent properties of $Ca_3(PO_4)_2(SiO_4)$: Eu^{2+} green-emitting phosphor for white light emitting diodes. *Opt. Commun.*, **289**, 103–108.

Received 14 May 2015
Modified version received 29 June 2015
Accepted 30 August 2015